High-throughput single-molecule experiments reveal heterogeneity, state switching, and three interconnected pause states in transcription

Janissen, Richard; Eslami-Mossallam, Behrouz; Artsimovitch, Irina; Depken, Martin; Dekker, Nynke H.

Important note
To cite this publication, please use the final published version (if applicable).
Please check the document version above.

Article
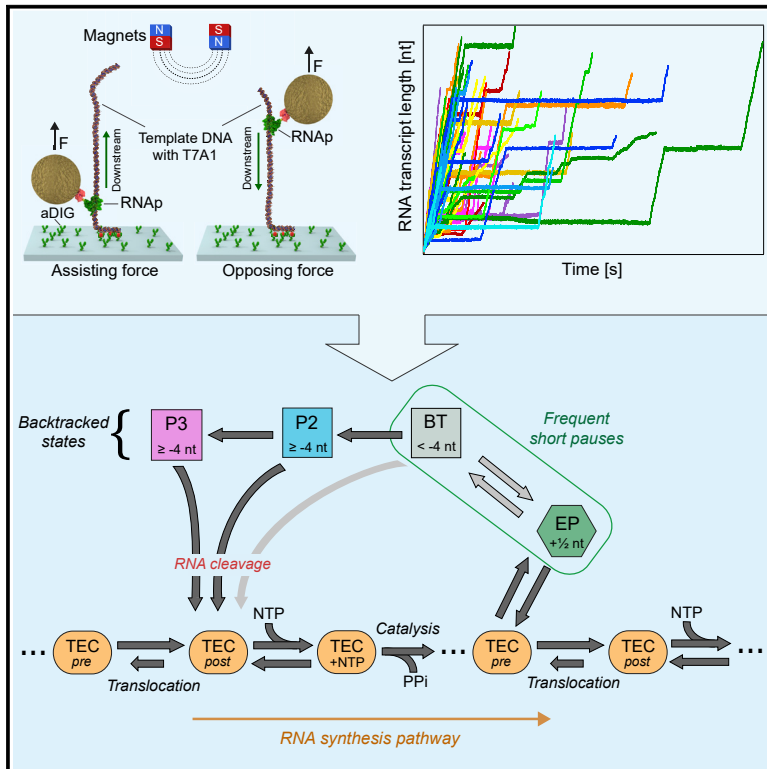
High-throughput single-molecule experiments reveal heterogeneity, state switching, and three interconnected pause states in transcription

Graphical abstract

Highlights

- Three intrinsic transcriptional pause states compete with transcript elongation

- Recovery from deep backtracks is governed by intrinsic RNA cleavage

- Elongation rate heterogeneity originates from alterations in short-pause frequency

- The consensus mechanistic model unifies biochemical and single-molecule observations

Authors

Richard Janissen,
Behrouz Eslami-Mossallam,
Irina Artsimovitch, Martin Depken,
Nynke H. Dekker

Correspondence

artsimovitch.1@osu.edu (I.A.),
s.m.depken@tudelft.nl (M.D.),
n.h.dekker@tudelft.nl (N.H.D.)

In brief

Combining single-molecule experimentation with computational modeling, Janissen et al. capture *Escherichia coli* RNAp-pausing dynamics on timescales from milliseconds to hours. They identify two long-lived pause states that compete with elongation and recover via nascent RNA cleavage. The authors provide a consensus mechanistic model unifying biochemical and single-molecule observations.

CellPress

Article

High-throughput single-molecule experiments reveal heterogeneity, state switching, and three interconnected pause states in transcription

Richard Janissen,[1,3] Behrouz Eslami-Mossallam,[1,3] Irina Artsimovitch,[2,*] Martin Depken,[1,*] and Nynke H. Dekker[1,4,*]

[1]Department of Bionanoscience, Kavli Institute of Nanoscience, Delft University of Technology, 2629 HZ Delft, The Netherlands
[2]Department of Microbiology, Ohio State University, Columbus, OH 43210, USA
[3]These authors contributed equally
[4]Lead contact
*Correspondence: artsimovitch.1@osu.edu (I.A.), s.m.depken@tudelft.nl (M.D.), n.h.dekker@tudelft.nl (N.H.D.)
https://doi.org/10.1016/j.celrep.2022.110749

SUMMARY

Pausing by bacterial RNA polymerase (RNAp) is vital in the recruitment of regulatory factors, RNA folding, and coupled translation. While backtracking and intra-structural isomerization have been proposed to trigger pausing, our mechanistic understanding of backtrack-associated pauses and catalytic recovery remains incomplete. Using high-throughput magnetic tweezers, we examine the *Escherichia coli* RNAp transcription dynamics over a wide range of forces and NTP concentrations. Dwell-time analysis and stochastic modeling identify, in addition to a short-lived elemental pause, two distinct long-lived backtrack pause states differing in recovery rates. We identify two stochastic sources of transcription heterogeneity: alterations in short-pause frequency that underlies elongation-rate switching, and variations in RNA cleavage rates in long-lived backtrack states. Together with effects of force and Gre factors, we demonstrate that recovery from deep backtracks is governed by intrinsic RNA cleavage rather than diffusional Brownian dynamics. We introduce a consensus mechanistic model that unifies our findings with prior models.

INTRODUCTION

The transcription of genetic information is the first step in gene expression. The synthesis of RNA transcripts is carried out by DNA-dependent RNA polymerases (RNAp), whose structures and molecular mechanisms are conserved throughout all domains of life (Lee and Borukhov, 2016). Transcription is a controlled process that defines cell identity, fitness, proliferation, and response to environmental signals. The RNAp itself is subjected to many forms of regulation, which include interactions with accessory proteins, nucleic acid signals, and small molecules inducing conformational changes in the active site and global structural changes in the transcription elongation complex (TEC) (Belogurov and Artsimovitch, 2019).

Pioneering work on bacterial RNAp revealed that RNA chain elongation is frequently interrupted by pauses that reduce the overall transcription velocity (Chamberlin et al., 1979; Maizels, 1973). Subsequent studies (reviewed in Kang et al., 2019), identified two types of pauses: sequence-induced regulatory pauses that allow timely interaction with transcription factors and the ribosome, and stochastic pauses originating from intrinsic random events within the enzyme (e.g., structural isomerization, misincorporation). Different single-molecule studies have identified a ubiquitous elemental pause (EP) state, *cis*-acting consensus DNA sequences, and interruption of RNA chain elon-

gation induced upon RNAp backtracking (also in eukaryotic Pol II) (Abbondanzieri et al., 2005a; Dangkulwanich et al., 2014; Gabizon et al., 2018; Galburt et al., 2007; Herbert et al., 2006; Lass-Napiorkowska and Heyduk, 2016). While short ~1-s pauses have been identified as signatures originating from the EP, longer pauses comprise a heterogeneous class of intermediates (Neuman et al., 2003; Saba et al., 2019). Apart from rare RNA hairpin-stabilized pauses, long-lived pauses are commonly attributed to backtracked RNAp. Gre factor-mediated cleavage of the nascent RNA is known to facilitate recovery from backtracked states, but biochemical studies of *E. coli* RNAp also emphasized the role of intrinsic cleavage and proposed the existence of two distinct backtrack states that differ in intrinsic cleavage rates, ~5 and ~100 s (Artsimovitch and Landick, 2000; Miropolskaya et al., 2017; Saba et al., 2019; Sekine et al., 2015). Similarly, eukaryotic Pol II recovers from deeper backtracks predominantly by RNA cleavage rather than by diffusional Brownian motion (Lisica et al., 2016). However, most single-molecule studies have attributed all pauses exceeding 5 s to a single state with a broad power-law distribution of pause durations that originate from diffusive TEC dynamics during RNAp backtracking and view this diffusional Brownian motion as the main recovery pathway (Dangkulwanich et al., 2014; Depken et al., 2009; Gabizon et al., 2018; Galburt et al., 2009; Mejia et al., 2008, 2015). Due to these divergent interpretations of
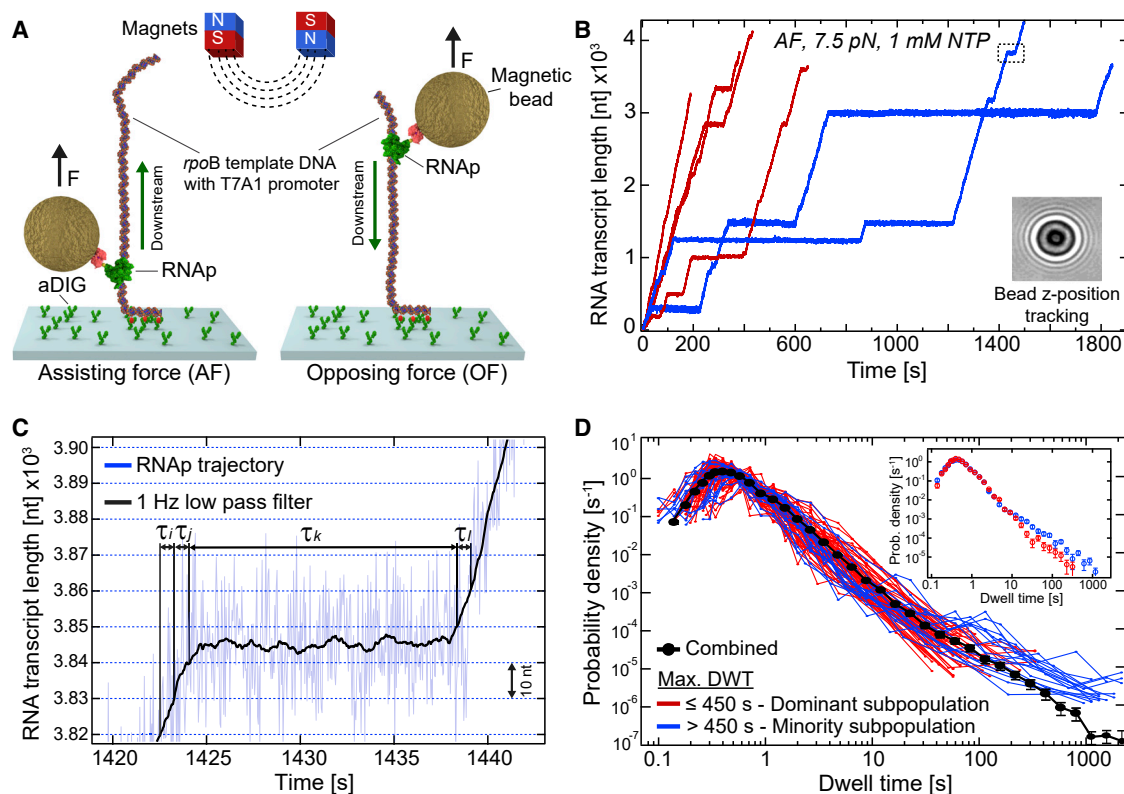
Figure 1. Single-molecule RNAp transcription dynamics reveals notable heterogeneity

(A) The magnetic tweezers *in vitro* transcription assay in the AF and OF configurations with respect to the RNAp downstream direction.

(B) Example trajectories of individual RNAps. Translocation was measured via the change of the bead diffraction pattern (inset) over time. Individual trajectories are colored based on their largest pause duration (red: ≤450 s; blue: >450 s; STAR Methods), M4.

(C) Magnified trajectory of region within the dashed rectangle in (B). Dwell times (τ_i, τ_j, τ_k, τ_l) associated with RNAp advancing through windows of several nucleotides (10-nt windows example shown with blue dashed lines) were extracted from 1-Hz-filtered trajectories (black line).

(D) Superimposed DWT distributions from individual trajectories (blue, red) and the combined DWT distribution of all trajectories (black, N = 196). The inset depicts the combined DWT distributions of the two subpopulations. Data in (B) and (C) were obtained under 7.5 pN AF at 1 mM NTPs.

See also Figure S1.

pause signatures from bulk and single-molecule experiments, a consensus mechanistic model describing intrinsic transcriptional pausing and backtrack recovery for RNAp remains lacking.

Previous single-molecule studies may not have fully captured infrequent pause states within limited observation times. Here, we employed high-throughput magnetic tweezers to probe the full temporal spectrum of *E. coli* RNAp transcription dynamics over a time period exceeding 2 h. Through dwell-time (DWT) analysis and simulation-based maximum-likelihood (ML) parameter estimation—which accounts for colored experimental noise and effects of trace smoothing—we identified and characterized three distinct pause states competing with elongation: a short-lived pause of ~1 s, which resembles the EP, and two long-lived, serially connected pause states, with lifetimes of ~4 and ~100 s, that branch from the EP. We show that the recovery from backtracks ≥4 nt is dominated by intrinsic RNA cleavage and not by diffusional Brownian motion, and that a subset of paused TECs assumes a conformation in which intrinsic and GreB-assisted RNA cleavage are hindered, delaying the escape to productive elongation. Our large datasets further allowed us to investigate the poorly understood heterogeneity in transcription velocity

and pause dynamics, providing evidence for previously postulated state switching (Neuman et al., 2003; Tolić-Nørrelykke et al., 2004) and demonstrating that it derives from stochastic alterations in the frequency of short pauses. By integrating these key findings with the results of previous studies, we present a unified mechanistic model that fully describes the origin and hierarchy of intrinsic pause states.

RESULTS

RNAp transcription dynamics exhibits notable heterogeneity

To capture infrequent events potentially missed by previous investigations, we established a single-molecule assay (STAR Methods, M1), based on high-throughput magnetic tweezers (STAR Methods), M2, that provides large datasets suited to statistically robust analysis (Cnossen et al., 2014; Dulin et al., 2015a). Halted TECs were formed by nucleotide deprivation, as described previously (Janissen et al., 2018), on surface-attached linear DNA template free of known pause-inducing sequences that could overshadow the intrinsic RNAp-pausing dynamics (Gabizon et al.,

2018; Herbert et al., 2006; Larson et al., 2014). By attaching magnetic beads to singly biotinylated RNAps and varying the DNA template orientation (Figure 1A), we could apply assisting forces (AF) or opposing forces (OF) to the RNAps while monitoring the progression of single RNAps along 40–60 DNA templates simultaneously in real time. Transcription was restarted upon the addition of all four nucleotides and monitored for $\geq$2 h at constant force.

In agreement with previous studies, the RNAp trajectories (Figure 1B) exhibited periods of apparently constant velocities punctuated by pauses of different duration and position (Janissen et al., 2018; Neuman et al., 2003). We constructed DWT distributions (Figure 1C) obtained for all trajectories (Dulin et al., 2015a) by measuring the time needed for each individual RNAp to successively transcribe a fixed number of nucleotides (STAR Methods), M3. With the extracted DWTs, we then performed a probabilistic analysis of RNAp kinetics sampled from 100 ms up to 2 h and extracted the underlying kinetic parameters (Dulin et al., 2015a; 2015b).

Figure 1D depicts individual example DWT distributions for trajectories measured under 7.5 pN AF at 1 mM [NTPs]. All individual DWT distributions qualitatively exhibit the same features: a peak at short time scales ($\sim$400 ms for the example shown) and a tail of gradually decreasing probability for DWTs >1 s. Whereas the peak reflects pause-free elongation, the tail originates from pauses. We observed a significant variation between individual DWT distributions (Figure 1D), particularly in the occurrence of extremely long-lived pauses. Whereas for the majority of trajectories all pauses lie well below 450 s, for $\sim$10% of trajectories the pauses extend to few thousand seconds. We found that the minority subpopulation exhibited an increased incidence of both extremely long (>450 s) and shorter (<10 s) pauses (Figure 1D, inset), indicating that these trajectories belonged to a distinct subpopulation of RNAps. As a result, the combined DWT distribution (Figure 1D, black), constructed by accumulating measured DWTs from all single trajectories without any preselection, was not representative of any of the individual DWT distributions. To reveal differences between these subpopulations, we used the Bayes-Schwarz information criterion (BIC) (Figures S1A–S1C) to estimate the number of single-rate pause states in the combined DWT distribution and in the DWT distributions corresponding to each subpopulation (Press et al., 2007; Schwarz, 1978). We found that whereas the pausing dynamics of each subpopulation can be captured with three single-rate pause states, the combined DWT distribution requires the incorporation of a fourth pause state, an artifact arising from combining two inherently different distributions. Since we found that the maximum pause duration provides a parameter that can successfully discriminate between the two subpopulations, we established a selection protocol using the Gaussian mixture model approach, which classifies individual trajectories based on the longest pause they contain (STAR Methods), M4. We first analyze the majority subpopulation and dissect the minority subpopulation in the last section of the Results.

Intrinsic RNAp dynamics reflects three distinct pause states

Previous studies have shown that the EP can act as an intermediate state for less frequent "stabilized" pauses with extended lifetimes (Kang et al., 2019). All other intrinsic pause signatures were previously attributed to diffusive backtracking. However, our measured DWT distribution is incompatible with the simple power-law decay that associates diffusive entry to, and recovery from, backtracking (Figure 2A). The BIC analysis indicates the existence of three distinct pause states (Figures 2A, S1A, S2A; STAR Methods, M5 and M6). We therefore propose a working model (Figure 2) that includes a frequent short pause state (P1) and two additional rare pauses (P2, P3) of extended duration. RNA chain elongation consists of several sub-processes including NMP addition, NTP hydrolysis, PP$_i$ release, and translocation, characterized by an effective elongation rate k_{el}, the inverse of the average time it takes to complete one NMP-addition cycle, conditioned on RNAp not entering a pause (see also discussion of k_{el} related to Figure 3D). It thus has non-exponential transition times to both pausing and subsequent elongation. We assume that a typical time associated with entering a pause is much shorter than the time to exit a pause and ignore it in what follows. We thus only consider the probability of leaving the elongation pathway and entering the off-pathway (through P1), denoted by P_{total}. The three pause states (P1, P2, and P3) are connected sequentially, jointly forming a single off-pathway branch; the entry into P2 and P3 is governed by the rates k_{P2} and k_{P3}, respectively, and all pauses return to the elongation pathway through the exit rates k_{e1}, k_{e2}, and k_{e3}.

Although many other pause configurations could explain any of the datasets, we now proceed to rule these out by demanding that our model be simultaneously consistent with a wide variety of experimental conditions. First, we parameterized the working model by fitting it to a combined DWT distribution, constructed from a large (361.3 kb of total transcript length; Table S1) reference ensemble of trajectories measured under 7.5 pN AF at a saturating [NTPs] of 1 mM. Under these conditions, the characteristic pause times are well separated from the pause-free elongation peak (Figure 2A), which allows for accurate ML estimation of all parameters (STAR Methods, M6; Figures 2B, 2C; Table S2) (Dulin et al., 2015a). The parameter values estimated from this dataset will be referred to as reference parameters hereafter. Having confirmed that the fit remains robust and is independent of the DWT-window size (we evaluated 4, 10, and 20 nt DWT window sizes; Figures S2B and S2C), we chose a 4-nt window for all subsequent analyses.

We found that the model captures well the velocity distribution (Figures S2D and S2E; STAR Methods), M7 used in previous studies (Forde et al., 2002; Gabizon et al., 2018; Larson et al., 2011; Mejia et al., 2015). The estimated k_{el} (Figure S2F) from the velocity distribution (k_{el}: 21.6 $\pm$ 0.2 nt/s) is compatible both with the value we obtain from DWT-distribution analysis (k_{el}: 21.7 $\pm$ 1.8 nt/s) and with reported pause-free velocity estimations (Larson et al., 2011; Mejia et al., 2015). Similarly, the lifetime of $\sim$1 s for P1 is similar to that of the EP, and pause lifetimes compatible with our estimates of $\sim$4 s (P2) and $\sim$100 s (P3) have also been reported (Artsimovitch and Landick, 2000; Mejia et al., 2008; Miropolskaya et al., 2017; Pupov et al., 2008; Saba et al., 2019).

We next investigated the variation in transcription velocity, defined as the velocity observed between longer pauses (P2 and P3). We removed all DWTs >4 s (which encompasses the P2 and P3 lifetimes) and then calculated the displacement of RNAp in
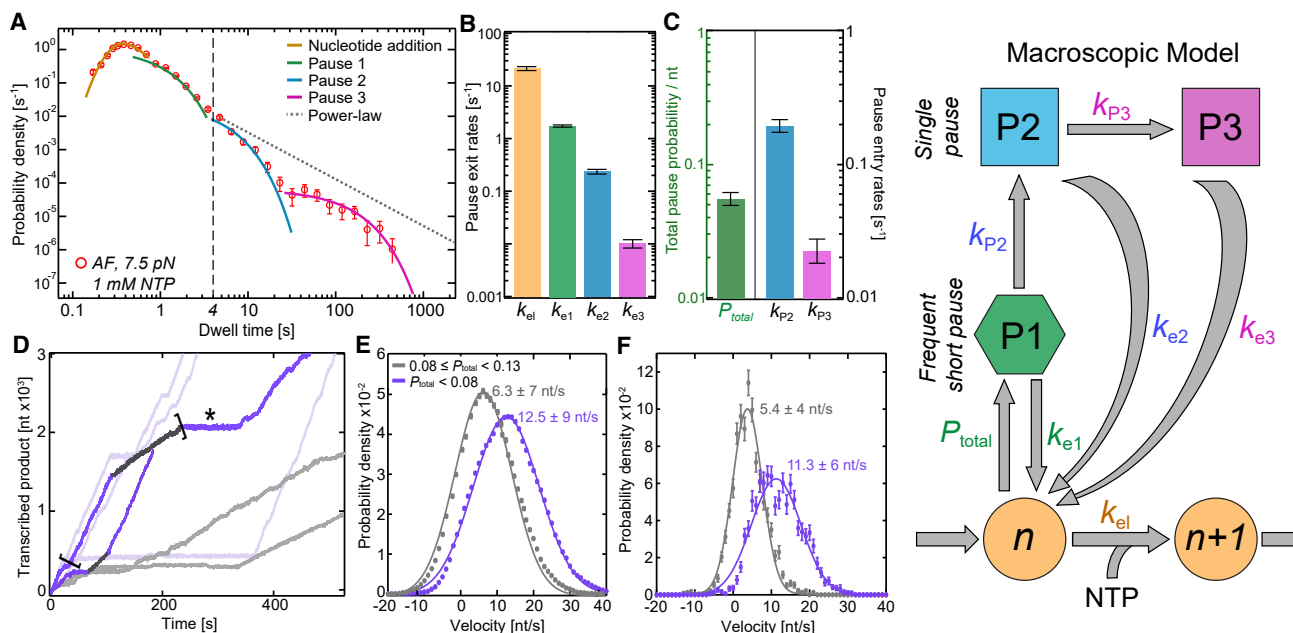
Figure 2. Analysis and extraction of kinetic values of RNAp transcription dynamics

(A) DWT distribution (red circles) for N = 177 trajectories measured at 7.5 pN AF at 1 mM NTPs. Solid curves show the best fit of the model (rightmost) to the dataset and are colored accordingly: orange represents pause-free elongation; green, cyan, and magenta the three exponential pauses P1, P2, and P3, respectively. The dashed vertical line depicts the pause lifetime threshold of 4 s. The gray dashed line illustrates a power-law distribution expected from diffusive backtracking dynamics.

(B and C) Values (±SD) shown of the model parameters from fitting the model to the DWT distribution in (A).

(D) Trajectories showing stochastic switching of velocity (dark colors). State switching is not detectable in most trajectories (light shades), although a significant variation in velocities (between purple and gray trajectories) is evident.

(E) Distribution of velocities (±SD) for the two groups of trajectories, separated by their estimated pause probabilities (P_{total}).

(F) Velocity distribution (±SD) obtained for two segments of a single trajectory (*) from D (within brackets). Solid lines and values in (E) and (F) show the best Gaussian fits.

See also Figures S1, S2, and S3.

consecutive temporal windows of 1 s. We also estimated the values of k_{el} and P_{total} for individual trajectories in the reference dataset (Figure S3A; STAR Methods), M7. An interesting feature is the lack of correlation between the estimated values of k_{el} and P_{total} (r = 0.16854). This can be explained by the consideration that these parameters depend on the subreactions in the elongation pathway in different ways: whereas P_{total} is mostly affected by transitions between the pre-translocated and the post-translocated state, k_{el} is dominated by the rate-limiting (i.e., slowest) step along the pathway. Under high AF of 7.5 pN and saturating [NTPs], where the transition between the pre- and the post-translocated state is not rate limiting and biased toward the post-translocated state, the variations in k_{el} and P_{total} can be uncorrelated. This implies that the observed variations in k_{el} most likely derive from heterogeneity in the rate of the NMP-addition rate k_c (Figure S4B), while the variations in P_{total} are related to the differences in pre/post-translocation rates and/or the pause entry rate. Whereas the distribution for k_{el} is largely symmetric, the distribution for P_{total} is skewed and bimodal; the transcription velocity distribution will consequently also be bimodal. Such bimodal transcription dynamics are also clearly evident in individual trajectories (Figure 2D), as previously reported (Abbondanzieri et al., 2005a). To characterize the heterogeneity in velocity, we analyzed two groups of trajectories conditioned on their estimated pause probabilities (i.e., $P_{total} < 0.08$ and $P_{total} > 0.08$). While RNAps in the first group show an average velocity of ∼10 nt/s (Figures 2D and 2E; purple), those in the second group advance at ∼5 nt/s (Figures 2D and 2E; gray). Interestingly, we also detected a small fraction of RNAp (<5%) in which the velocity alternated between these velocities, a phenomenon indicative of state switching (Davenport, 2000; Harrington et al., 2001). The lack of a clear correlation between k_{el} and P_{total} for individual trajectories (Figure S3A) implies that the division of the trajectories into two groups based on their pause probabilities does not affect the distribution of the effective elongation rates in each group. We therefore conclude that the variations in the frequency of short pauses, and not changes in k_{el}, underlie the observed heterogeneity.

We next asked how representative the combined DWT distribution is for the dynamic behavior of individual RNAps. We found that although k_{el} and P_{total} exhibit rather wide distributions, the combined DWT distribution that includes all trajectories (Figure S3D) can be described well by their average values, as expected by the law of averages. This establishes that, despite the inherent heterogeneity found in model parameters, fitting the combined DWT distribution results in a population-averaged estimation of the parameters.
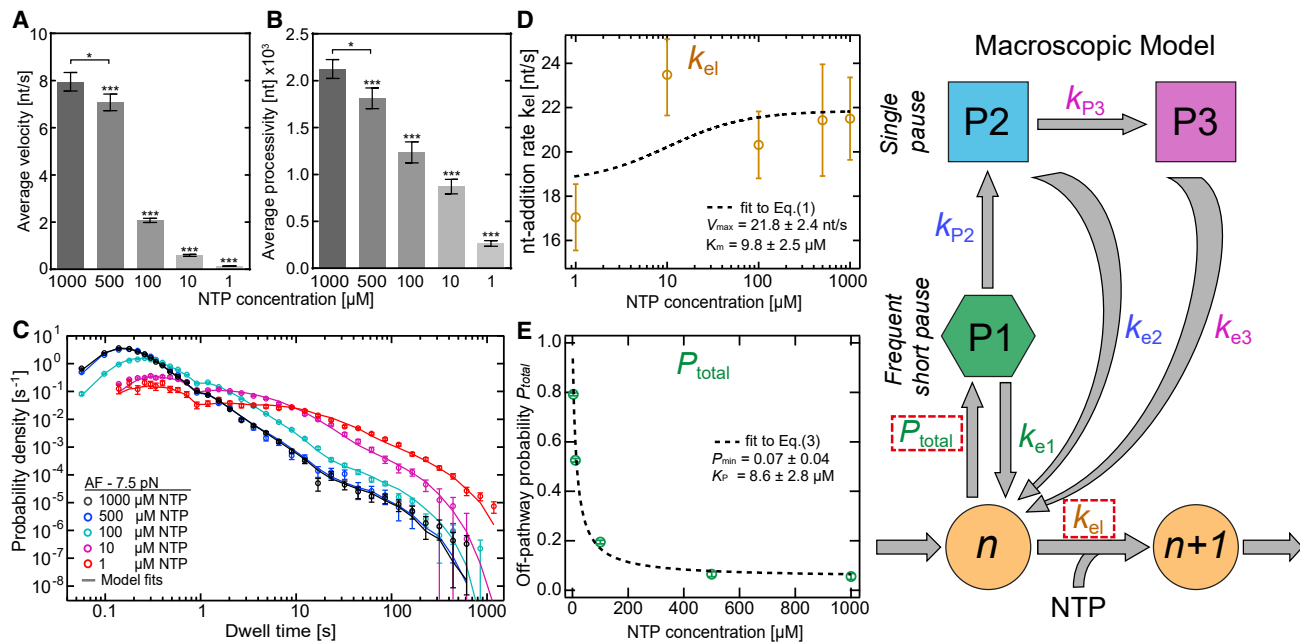
Figure 3. NTP deficiency increases pausing probability and reduces effective elongation rate

(A) Measured average (±SEM) end-to-end velocity and (B) average processivity (±SEM) at different [NTPs].

(C) Superimposed DWT distributions (circles) at different [NTPs]. The lines represent the best two-parameter fit of the model (rightmost) to each dataset by setting only k_{el} and P_{total} as free fit parameters (dashed rectangles).

(D) Effective k_{el} from (C), fitted with Equation (1) (dashed line).

(E) Off-pathway entry probabilities P_{total} resulting from the fits to datasets in (C), fitted with Equation (3) (dashed line).

See also Figure S4.

All pauses compete with nucleotide addition

To validate the structure of our working model, we first wished to establish whether all three identified pause states compete with the active elongation pathway. To do so, we measured the response to [NTPs] ranging from 1 to 500 μM at a constant force of 7.5 pN AF. Overall, in agreement with previous results obtained from bulk and single-molecule experiments, we found that the NTP deficiency reduced the average transcription velocity significantly (Figure 3A), resulting in a proportional decrease in the processivity of TECs (Figures 3B and S4A) due to the unchanged TEC lifetime (Figure S4A) (Abbondanzieri et al., 2005a; Forde et al., 2002; Mejia et al., 2015).

As the [NTPs] decreases, the elongation peak in the combined DWT distributions (Figure 3C) shifts to larger DWTs, indicating a slower k_{el}. At the same time, the probability of all pauses gradually increases, suggesting that all three pauses are off-pathway states in (possibly indirect) competition with nucleotide addition. For the working model (Figure 3, rightmost) to be true, the dataset obtained at different [NTPs] should be fully captured by allowing only k_{el} and P_{total} to vary while keeping all other parameters fixed (Table S2). As a validation, we used this approach (STAR Methods), M8 to fit our model to the empirical DWT distributions measured at varying [NTPs]. The resulting two-parameter fits (Figure 3C, solid lines) fully capture the observed NTP-dependent variations in the combined DWT distributions.

We next investigated the [NTP] dependency of both k_{el} and P_{total}. Previous single-molecule studies often attempted to

measure k_{el} by exclusively focusing on the active pathway and excluding pauses longer than a certain threshold (Abbondanzieri et al., 2005a; Dangkulwanich et al., 2014; Depken et al., 2009; Forde et al., 2002; Gabizon et al., 2018; Herbert et al., 2006; Mejia et al., 2008). However, we note that the mere existence of a competing pause branch affects the lifetime associated with the elongation pathway and that this effect would still be present even if all the pauses were excluded. Taking this into account (STAR Methods), M9, k_{el} is given by

$$k_{el} = \left(1 + \frac{K_p}{[\text{NTP}]}\right)k_{el}^0, \quad \text{(Equation 1)}$$

where the term in the parentheses represents the effect of the pause branch, with K_p given in terms of microscopic rates by Equation S34 (STAR Methods), M9, and k_{el}^0 follows the Michaelis-Menten kinetics expected in the complete absence of a pause branch (Neuman et al., 2003)

$$k_{el}^0 = V_{max}\frac{[\text{NTP}]}{[\text{NTP}] + K_m}. \quad \text{(Equation 2)}$$

Equations 1 and 2 imply that k_{el} saturates at a finite value at very low [NTPs]. This can be understood by considering that $1/k_{el}$ represents the lifetime of the on-pathway elongation conditioned on *not* pausing: even if the NMP-addition rate is
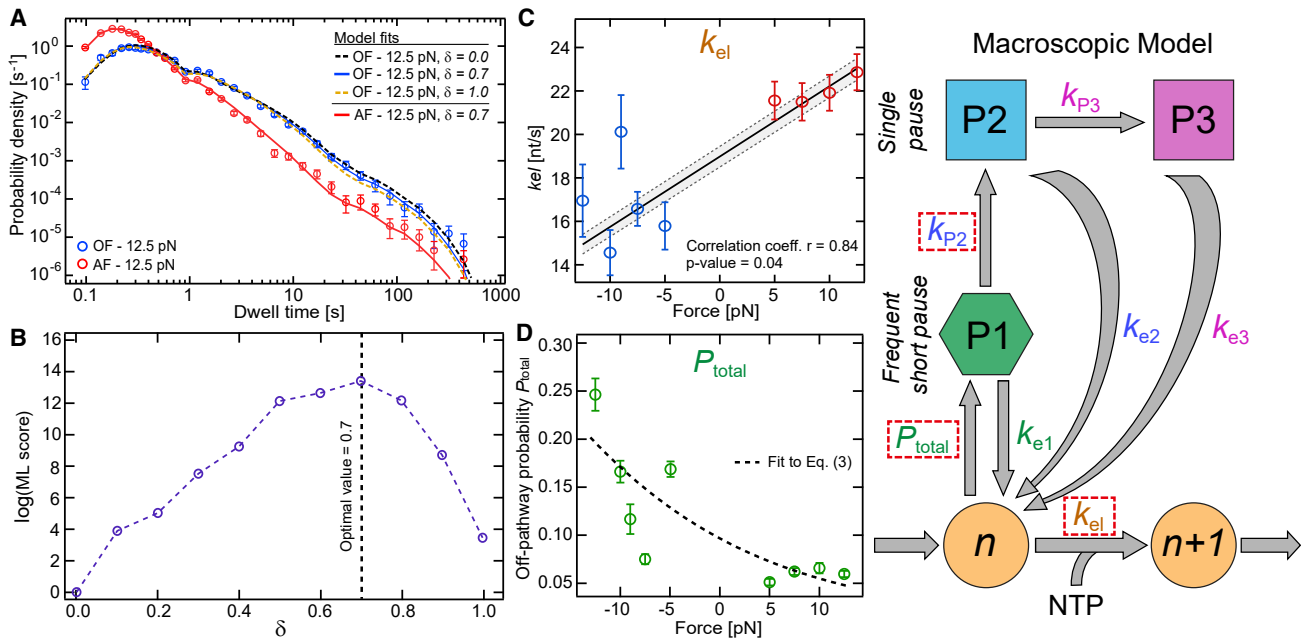
Figure 4. RNAp backtracking exhibits force dependency in the entry rate

(A) Combined DWT distributions at 12.5 pN AF and OF. The (dashed) lines represent the best fits of the model (rightmost) to each dataset. Three fit parameters, k_{el}, P_{total}, and k_{P2}, assumed force dependent by the parameter δ (δ = 0: maximal force dependency, δ = 1: no force dependency; Equation 4), were used.

(B) Fit quality as a function of δ, from fitting the OF 12.5 pN dataset in (A).

(C and D) k_{el} (±SEM) and P_{total} (±SEM), respectively, from the fits to datasets at different applied forces. The line in (C) represents a linear regression fit (dashed lines: ±SD) to the data, and the legend denotes the Pearson correlation coefficient r and p values (significance level α = 0.05). The dashed line in (D) depicts the theoretical prediction (Equation 3) with δ = 0.7.

See also Figures S4, S5, and S7.

very low, only translocation steps fast enough to occur prior to pausing will contribute to the lifetime. The value of k_{el} remains finite for the contributing subpopulation, while the size of the population shrinks as the pause probability approaches unity at the lowest [NTPs],

$$P_{total} = \frac{P_{min} + K_p/[NTP]}{1 + K_p/[NTP]}. \qquad \text{(Equation 3)}$$

In the equations above, the parameters V_{max}, K_m, K_p, and P_{min} depend only on the rates that constitute the active pathway and on the entry rate into the pause branch (Figure S4B; STAR Methods), M9. Their precise values are expected to vary for different NTPs (Abbondanzieri et al., 2005a; Prajapati et al., 2019; Yuzenkova et al., 2010). We found that the values of k_{el} and P_{total} estimated by the fits are well captured by Equations 1 and 3 (Figures 3D and 3E), leading to averaged (over 4 nt, based on the DWT window) estimations of V_{max} = 21.8 ± 2.4 nt/s, K_m = 9.8 ± 2.5 μM, K_p = 8.6 ± 2.8 μM, and P_{min} = 0.07 ± 0.04. The model remains consistent with the empirical DWT distributions even if K_m is increased to 100 μM, compatible with K_m values previously measured for different individual NTPs. Thus, our estimated value of K_m should be considered a lower bound for the averaged Michaelis-Menten constant. Deviations between the data and model predictions occur only in the left tail of the DWT distributions (Figure S4C;

i.e., at DWTs <0.2 s), which is most sensitive to (and can be biased by) experimental noise.

Recovery from deep backtracks is dominated by intrinsic cleavage

We next investigated the origin and interconnection of pause states. Previous studies associated longer pause lifetimes with diffusive return from backtracking, which should be susceptible to force. We systematically measured the transcription dynamics at applied forces ranging from 5 to 12.5 pN in AF and OF orientations (Figure S5) at 1 mM [NTPs]. As the OF is increased, we globally observe a substantial decrease in the average velocity (Figure S5A) and TEC processivity (Figure S4A), indicating a change in either k_{el}, P_{total}, pause lifetimes, or a combination thereof. Figure 4A depicts DWT distributions measured at 12.5 pN in AF and OF (DWT distributions for all forces are shown in Figures S5B and S5C). We found that switching the force direction from AF to OF produces an effect similar to that observed at low [NTPs]: enhanced pausing probability accompanied by a decrease in k_{el}.

To explain this force dependency, we first fitted our model (Figure 4, rightmost) to the 12.5 pN OF dataset by allowing only k_{el} and P_{total} to change while fixing all other parameters to the reference values (Figure 4A, yellow dashed line). Although the model fits the data at short timescales, <10 s, it slightly

deviates at longer timescales. This remaining discrepancy vanishes when we introduce force dependence in the entry rate of the P2 state as

$$k_{P2} = k_{P2}^{ref} \exp\left(-\frac{(F - F^{ref})(1 - \delta)a}{k_B T} \right), \qquad \text{(Equation 4)}$$

where $a \approx 0.37$ nm is the average step size of RNAp, k_{P2}^{ref} is the value corresponding to the reference force $F^{ref} = 7.5$ pN, δ identifies the position (in nt) of the transition state between pre-translocated and backtracked states, and F is the applied external force (Abbondanzieri et al., 2005b; Depken et al., 2009). By sweeping the range for δ between 0 and 1 (STAR Methods), M8, we found that the entry to P2 exhibits force dependency with an optimal value of $\delta \sim 0.7$ (Figure 4B). Correspondingly, maximizing the force dependency of k_{P2} by setting $\delta = 0$ results in an overestimation of the probability of the long-lived pauses P2 and P3 (Figure 4A, black dashed line).

To validate proposed force dependency for k_{P2}, we performed two-parameter fits to the datasets obtained at different forces by using k_{el} and P_{total} as fit parameters, fixing k_{P2} at its expected value for each force assuming $\delta = 0.7$ (Equation 3; Figure S5D) and fixing all other model parameters to their reference values (Table S2). The resulting fits to the data at 12.5 pN AF (Figure 4A, red solid line), as well as to all other measured forces (Figures S5B and S5C), demonstrate that our model remains valid at different forces.

We next explored the force dependency of the elongation pathway. Each NMP-addition cycle involves forward translocation of RNAp, which is expected to be affected by force (Abbondanzieri et al., 2005a). We found that k_{el}, as estimated by our fits, is slightly force dependent (Figure 4C), implying that at saturating 1 mM [NTPs] translocation can become rate limiting across the studied force range. Similarly, the off-pathway pause probability P_{total} shows an increasing trend as the force is gradually swept from AF to OF (Figure 4D). This observation indicates that pausing is in competition with translocation, justifying our assumption that the entire pause branch originates from the pre-translocated state.

Using Equation S36 (STAR Methods), M9 to describe the force dependency of P_{min} and K_p in Equation 3 with the reference values $P_{min}^{ref} = 0.07$ and $K_p^{ref} = 8.6$ μM corresponding to the force $F^{ref} = 7.5$ pN (Figure 3E), and assuming that the force dependence of P_{total} is due only to the reduction in the rate of the competing reaction in the forward elongation cycle, we fitted Equation 3 to the estimated values of pause probability (Figure 4D). The best fit corresponds to $\Delta \approx 0.5 \pm 0.16$, which identifies the position of the transition state (Equation S35, STAR Methods), M9 along the elongation pathway. We note that around 5 pN OF a non-monotonic variation of the pause probability gives some discrepancy with the model prediction. Possibly, this results from an inhomogeneity in the magnitude of force applied to the different magnetic beads (Ostrofet et al., 2018).

The entry rate k_{P2} into the first longer-lived pause P2 increases with OF (Figure S5D), prompting us to propose that P2, and in consequence, P3 are backtracked pauses; RNAp can stochastically switch to an inactive, backtrack-prone mode (Komissarova and Kashlev, 1997; Nudler et al., 1996). In a backtracked TEC, the nascent RNA is threaded through the active site, blocking NMP addition. The RNAp can recover, restoring the 3′ end to the active site, either by diffusing forward or by cleaving the backtracked RNA (Belogurov and Artsimovitch, 2019).

We investigated whether, as commonly thought, the force dependency reflected in our data could be explained by diffusive backtrack recovery. Evident from our analysis, and in agreement with other reports (Mejia et al., 2008, 2015), the P2 and P3 lifetimes are insensitive to external forces. This effect has been previously rationalized in terms of a force-independent $t^{-3/2}$ power-law region in the DWT distribution, a signature attributed to diffusive backtrack recovery (Depken et al., 2009). This power-law behavior, however, will eventually transform into an exponential cut-off at large external forces or long observation times, which is also apparent in our data at extended DWTs (Figures 4A, S5B, and S5C), and motivated us to assess (STAR Methods), M10 the compatibility of the diffusive backtracking model over the full temporal range of our data (Figure S6). We found that this model captures the combined DWT distribution well, provided that the maximum backtrack depth (BT) exceeds 5 nt (Figure S6A). However, the agreement between the data and the model fails at high OFs, and none of the simulated DWT distributions (Figure S6B) satisfactorily captures the data. Moreover, the best-fit simulated trajectories typically show a significantly shorter processivity than the measured data, an inherent property of the diffusive backtracking model in which at sufficiently high OFs all RNAps will eventually be trapped in a deep backtrack (Figure S6C) (Depken et al., 2009). We found that this occurs when the maximum BT is >5 nt, leading to simulated trajectories that show, on average, a processivity at least one order of magnitude lower than the mean value deduced from our measurements collected over >2,000 s (Figure S6D). Thus, although the diffusive backtracking model can be fitted to any individual DWT distribution at a constant force, it does not provide a consistent description of our data over the entire force range and significantly underestimates RNAp processivity. Importantly, this strongly indicates that diffusive RNAp dynamics alone cannot account for the observed long-lived pauses in our empirical DWT distributions.

The intrinsic RNA cleavage provides an alternative pathway for recovery from backtracking by allowing RNAp to restart RNA chain extension upstream from the position where backtracking was initiated (Figure S7A). An external force can affect the backtrack depth reached before cleavage and could thus also affect the recorded dwell-time. However, if the time for a TEC to return to its original position after cleavage is much shorter than the time spent in the backtrack, then the apparent lifetimes of P2 and P3 would remain largely unaffected by force. Even at the lowest estimated effective k_{el} (17 nt/s at 12.5 pN OF), the time spent in backtracks is much longer than the time to return if cleaved: for a 20-nt deep backtrack, it takes <1 s to translocate back. Therefore, we reason that the backtrack recovery by cleavage would result in pause lifetimes that are robust against an OF. This notion is compatible with the observed lack of sensitivity of the P2 and P3 lifetimes to external force. We thus take both the force independence and the incompatibility of the
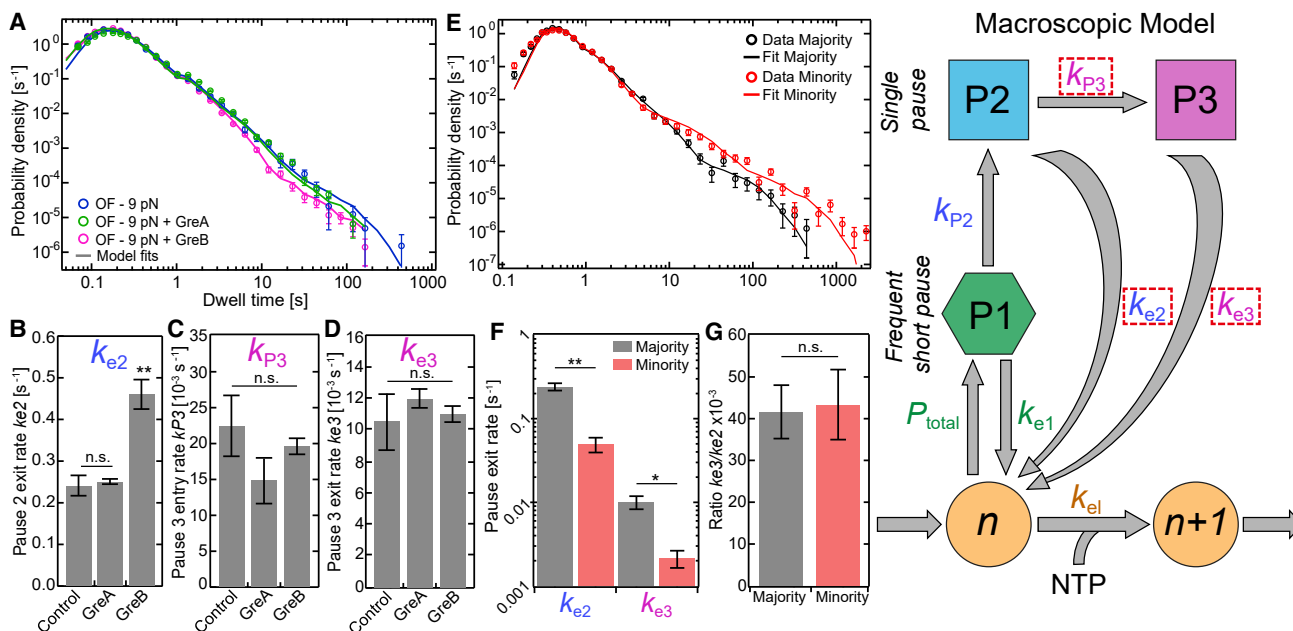
Figure 5. GreA/B-mediated cleavage and heterogeneity in intrinsic cleavage

(A) Superimposed combined DWT distributions at 9 pN OF in presence of GreA (green) or GreB (magenta), and absence of either (blue). The lines in (A) represent the best fits of the model (rightmost) to each dataset, using k_{e2}, k_{P3}, and k_{e3} as the only free fit parameters (dashed rectangles).

(B–D) (B) k_{e2}, (C) k_{P3}, and (D) k_{e3} estimated from the fits in (A).

(E) Superimposed DWT distributions (circles) and fits (lines) for the minority and majority subpopulations, extracted from the reference dataset and separated by Gaussian mixture clustering (STAR Methods), M4.

(F) k_{e2} and k_{e3} for the majority and minority subpopulations, estimated from the fits in (E).

(G) The ratio between k_{e2} and k_{e3} for the majority and minority subpopulations.

See also Figures S4 and S7.

diffusive backtrack model with our data as indications that intrinsic cleavage forms the main recovery pathway for the deep-backtrack states P2 and P3. In addition, the fact that P3 pauses are not associated with backtracks deeper than P2 (Figure S7B) provides further evidence that diffusive dynamics is irrelevant for these pause states.

Deep backtracked pause states are affected differently by Gre cleavage factors

We probed the contribution of RNA cleavage to backtrack recovery dynamics by using elongation factors GreA and GreB, which promote intrinsic cleavage in backtracked TECs (Borukhov et al., 1993; Sosunova et al., 2013). To increase the measurable effect of Gre factors, we applied an OF that favors the long-lived pauses (Figures 4, S5). Figure 5A shows the effect of 2 μM GreA or 2 μM GreB on the DWT distribution measured at 9 pN OF, 1 mM [NTPs]. It is evident that solely pauses exceeding 4 s (P2 and P3) are affected by Gre factors and that the effect is considerably more pronounced for GreB. We fitted our model (Figure 5) to the Gre factor datasets (STAR Methods), M8 by allowing only k_{e2}, k_{P3}, and k_{e3} to vary; all other model parameters were fixed according to the best fit to the corresponding control data acquired in the absence of Gre factors. We found that the three-parameter fits were able to fully capture the effects of both Gre factors (Figure 5A); the resulting fit values are shown in Figures 5B–5D. Compared with the control data, the effect

of GreA was statistically insignificant, whereas GreB significantly increased k_{e2} while leaving k_{P3} and k_{e3} unchanged within errors.

Since GreB facilitates recovery from deep, the observed acceleration of the exit rate k_{e2} indicates that the P2 pause originates from backtracked TECs. The concomitant reduction in the occurrence of the P3 pause state, reflected by a decrease in the population of pauses >10 s in Figure 5A, supports our assumption that the entry to P3 competes with recovery from P2, implying that P3 also originates from a backtrack-induced pause. BT analysis also reveals that P2 and P3 are associated with backtracks with similar depths >4 nt (Figures S7A and S7B). In contrast to P2, the lifetime of P3 (Figure 5D) is largely unaffected by GreB. This suggests that, to enter P3, P2-paused RNAp may undergo conformational changes that render it resistant to GreB-assisted cleavage, which in turn leads to a 20-fold slower recovery rate compared with the recovery from P2.

Our observation that GreA has a negligible effect on short pauses is in agreement with previous single-molecule studies (Shaevitz et al., 2003; Zlatanova et al., 2006) and could reflect the fact that GreA mainly affects backtracks of ≤3 nucleotides (Borukhov et al., 1993). This result indicates that shallow backtracks are short lived and either recover quickly (≤1 s) via rapid intrinsic cleavage or diffusion or lead to extended backtracking and could explain why short backtracks remain undetected in our analysis, as their contribution might be overshadowed by the EP (Saba et al., 2019).

A minority population reveals the nature of long-lived backtrack-associated pauses

As described above, variations in the duration of long pauses between individual RNAp trajectories (Figure 1D) allowed us to distinguish (STAR Methods), M4 a majority subpopulation (~90%), to which we fitted our working model, and a minority subpopulation (~10%), which contained trajectories with pauses exceeding thousands of seconds and has thus far been excluded from our analyses. Here, we ask whether the transcription dynamics in this minority subpopulation can be understood in the context of our model.

We constructed a combined DWT distribution using only the minority subpopulation from the reference dataset and performed a maximum-likelihood fit (Figure 5E) to obtain a new set of model parameters. We found that only the exit rates from P2 and P3 vary significantly between the minority and majority subpopulations (Figure 5F), while all other parameters remain statistically unchanged (Figure S7C). We note that the P2 lifetime is shorter than the 450-s cutoff used in the selection process and is thus not affected by the RNAp trajectory selection based on the duration of the longest pause. The fact that not only long P3 pauses but also shorter P2 pauses differ between the two subpopulations thus confirms that differences in their exit rates reflect an actual change in RNAp dynamics rather than artifacts imposed by our selection cutoff. Strikingly, the ratio between these exit rates is comparable in both subpopulations (Figure 5G), suggesting that rate-limiting subprocesses that form the P2 recovery pathway also dominate the P3 recovery, consistent with TEC escaping from both pause states by cleavage. Although P2 and P3 do not appear to differ in BT (Figure S7B), recovery from P3 occurs ~20 times slower and is not accelerated by GreB. These observations are consistent with P3 resulting from an infrequent, long-lived conformational change in backtracked TEC that must be reverted prior to RNA cleavage.

DISCUSSION

Based on *in silico* modeling of large datasets collected over many experimental conditions, we have provided a complete quantitative characterization of the full temporal spectra of RNAp pausing dynamics. We have established the hierarchical relations between transcriptional pauses and their origin, which confirm and unify previous observations made in isolation. We have provided evidence that the observed heterogeneity in average transcription velocity and the previously reported dynamic state switching are related, both originating from variations in the frequency of short pauses. We have further identified a cleavage-deficient subpopulation of RNAps that exhibit long-lived backtrack pauses. The characterization of this subpopulation, together with probing the effect of Gre factors on pausing dynamics, reveals two distinct backtrack pause states that differ in the intrinsic RNA cleavage rate. This discovery has allowed us to further elucidate the mechanism of recovery from deep backtracks and to rationalize the contradicting viewpoints presented in the literature.

A unifying mechanistic model of intrinsic transcription dynamics

On the basis of our findings, we propose a full kinetic model (Figure 6) in which frequent short-lived pauses, consisting of the EP and shallow backtracks of lifetimes <1 s, lead to two long-lived pauses (P2 and P3) accompanied by BTs >4 nt.

Our results are largely consistent with previous models that have assumed serially connected pause states (Abbondanzieri et al., 2005b; Lisica et al., 2016; Ó Maoiléidigh et al., 2011; Saba et al., 2019). The shortest pause of ~1 s resembles the EP, an off-pathway, half-translocated state that branches from the pre-translocated state. In this state, next-nucleotide loading is inhibited, and the RNAp can translocate relative to the template DNA by only ~0.5 nt (Kang et al., 2019; Saba et al., 2019). In addition to the EP, we demonstrated that the two long-lived pauses were promoted by OF and thus represent RNAp backtracking, but that their lifetimes were not affected by force. While the lack of force dependency has been attributed to a force-independent power-law tail of the DWT distribution that originates from diffusive backtracking, we also found that the diffusive backtracking model does not provide a consistent description for our data across the entire force range. Instead, our findings imply that the RNAp recovers from long-lived P2 and P3 pauses by RNA cleavage with rates observed in biochemical studies (Saba et al., 2019). Since P2 and P3 differ in their susceptibility to intrinsic and Gre-assisted RNA cleavage, we conclude that both pause states correspond to BTs exceeding ~4 nt and propose that they are separated by a conformational change in RNAp, as discussed below. The fact that BTs ≤4 nt remain undetected in our analysis implies that their recovery, whether through diffusion or through cleavage, is faster than, or comparable to, the EP.

The proposed kinetic model, with serially connected pause states and RNA cleavage as the predominant recovery mechanism from deep-backtrack states, also resembles the observations made for Pol II (Adelman et al., 2002a; Dangkulwanich et al., 2014; Kwak and Lis, 2013; Lisica et al., 2016). After entering the EP state, bacterial RNAp and Pol II can transition into backtracked states where the intrinsic cleavage acts as a potential recovery mechanism in kinetic competition with the Brownian diffusion. While both polymerases return from shallow backtracks mainly by diffusion, the intrinsic cleavage becomes dominant as the BT increases (Figure 6A). Deep backtracks cause a temporary RNAp arrest, from which recovery is possible only by transcript cleavage, either intrinsically or in conjunction with accessory elongation factors. The observation that the RNAp P2 and P3 states have vastly different lifetimes is similar to the proposed model for Pol II, with cleavage rate spanning a similar time range depending on the BT.

Our proposed consensus mechanistic model (Figure 6B) that unifies our and previous key findings will serve as a baseline for future studies on bacterial RNA synthesis, allowing for a quantitative characterization of effects of transcription factors, RNAp-targeting antimicrobials, among others, on transcription dynamics. By applying the presented statistical analysis to such studies, and comparing the outcomes with this baseline, it will be possible to identify the RNAp kinetic state(s) that the above-mentioned elements act on.

Figure 6. Unified mechanistic model of transcription elongation

(A) Schematic depiction of the TEC in the active pre- and post-translocated states, and in deep-backtracked states (P2 and P3). During elongation, the 3′ end of the RNA is aligned with the RNAp active site (*i* and *i+1*) but is increasingly displaced into the secondary channel during backtracking. RNAp can recover from shallow backtracks through 1D diffusion until the RNA 3′ end realigns with the active site ("pre"). Deep-backtracked configurations predominantly recover through RNA cleavage that generates a new 3′ end aligned with the active site ("post").

(B) The active pathway includes the pre-translocated ("pre"), post-translocated ("post"), NTP-bound ("+NTP"), and catalysis (with PP$_i$ release) states. The sub-processes involved in RNA elongation, translocation, NMP addition, and catalysis collectively contribute to the effective elongation rate k_{el}. The pause pathway includes the—half-translocated—EP, the—undetected—fast pause (BT) associated with backtracks < –4 nt, and two long-lived pauses (P2 and P3) associated with deep backtracks with cleavage-mediated recovery. For each pause state, the assumed position of the RNAp's active site with respect to the pre-translocated state is identified. The estimated maximum velocity (V_{max}; Equation 1) and lifetimes for each pause state, for the dominant subpopulation, are denoted in red.

The nature of long-lived backtrack-stabilized kinetic states

Our analysis has revealed that *E. coli* RNAp can fall into long-lived, cleavage-resistant pause states while transcribing a template that is free from known pause-inducing sequences (Gabizon et al., 2018; Herbert et al., 2006; Larson et al., 2014). Although TECs with similar properties have been reported in biochemical studies (Miropolskaya et al., 2017; Yuzenkova and Zenkin, 2010; Zhang et al., 2010), these complexes were assembled on short scaffolds and equilibrated for an extended time. Remarkably, the rate of RNA hydrolysis in *E. coli* TECs can vary over 60,000-fold (Miropolskaya et al., 2017), with TECs assembled on scaffolds containing an EP sequence or a deeply (~9 bp) backtracked RNA being particularly resistant to intrinsic and Gre-stimulated cleavage (Miropolskaya et al., 2017; Zhang et al., 2010). The arrest of RNAp in a cleavage-resistant state has also been observed in single-molecule investigations, where RNAp stalled through applied

force were found to be unable to resume transcription, even in presence of GreB (Forde et al., 2002; Yin et al., 1995), suggesting that conformational changes in the active site cause the mechanistically arrested state. Conformational transitions of several mobile RNAp domains, most notably the catalytic trigger loop (TL) and a large *E. coli*-specific SI3 insertion in the middle of TL, have been proposed to explain these differences (Miropolskaya et al., 2017; Yuzenkova and Zenkin, 2010; Zhang et al., 2010).

Recent cryo-EM structures of *E. coli* TECs stabilized in a paused state upon formation of an RNA hairpin (Guo et al., 2018; Kang et al., 2018) or by an engineered backtrack (Abdelkareem et al., 2019) confirmed these predictions. In inactive TECs, RNAp undergoes a rotational motion termed "swiveling," which repositions the TL and SI3 modules, preventing TL folding and thus inhibiting catalysis. A similar ratcheting motion accompanies the formation of a backtracked *Thermus thermophilus* TEC (Sekine et al., 2015). By contrast, catalytically competent

TECs, including a GreB-bound backtracked TEC poised for RNA cleavage (Abdelkareem et al., 2019), are not swiveled.

Swiveling is thought to accompany the formation of EP and long-lived regulatory pauses (Kang et al., 2019). Interestingly, our analysis reveals two distinct long-lived paused states, both of which are eventually able to resume transcription but differ significantly in their sensitivity to RNA cleavage. Since we and others (Abbondanzieri et al., 2005a; Bar-Nahum et al., 2005; Markovtsov et al., 1996; Mejia et al., 2008; Miropolskaya et al., 2017) failed to observe significant differences in the BT between GreB-sensitive (P2) and -resistant (P3) states, we hypothesize that P2 TECs can either stochastically revert to the elongation pathway through RNA cleavage or undergo additional conformational changes into the inert P3 state. Our results indicate that the majority of TECs that remain in the P2 state longer than $k_{p3}^{-1} \sim 1$ min will be found in the inert P3 state. This estimation is supported by studies that "walked" TECs into backtracked states of various BTs and stalled the RNAp for several minutes, reporting cleavage times comparable to our estimation of the P3 lifetime ($\sim$100–200 s).

While the triggers and structural changes that accompany P3 formation are not known, repositioning of the β' rim helices or SI, which directly contact GreB (Abdelkareem et al., 2019), or slight changes in the path of backtracked RNA (Markovtsov et al., 1996), would strongly affect endonucleolytic cleavage. The free RNA originating from deep backtracks could also act as a potential trigger by forming secondary structures, constraining diffusional return, and thereby favoring an inert state. Recovery from the inert P3 state would then require reversal of such additional changes and counter-swiveling into an active conformation. Future structural studies focusing on TEC stalling and factor-assisted cleavage may provide further insights into the properties of different backtrack states.

The origin of heterogeneity in transcription velocity and pausing dynamics

Most single-molecule studies aggregated all measured transcription trajectories, yet evidence in support of dynamic state switching, which involves alternation between different transcription velocities of a single RNAp, has also emerged (Davenport, 2000; Tolić-Nørrelykke et al., 2004). However, most studies failed to detect state switching, concluding that individual RNAps transcribe at a constant velocity, with apparent differences possibly due to arbitrary structural and chemical variations between RNAps that arise during their expression and assembly into an initiation-competent holoenzyme (Adelman et al., 2002b; Larson et al., 2011).

By capturing the full extent of temporal transcription dynamics, we observed considerable heterogeneity in elongation rates and pause frequencies for individual RNAp. Particularly, whereas the majority of RNAps transcribed at similar average velocities ($\sim$10 nt/s), a notable fraction of RNAp ($\sim$10%) translocated more slowly ($\sim$5 nt/s), and a small fraction ($\sim$5%) of RNAp trajectories showed switching between these two velocities. Strikingly, these velocities are quantitatively compatible with the previously described state switching (Davenport, 2000). Our analysis of RNAp trajectories with different average velocities indicates that state switching

originates from alterations in the frequency of short pauses, since the effective elongation rate remained unaffected.

The 2-fold difference in rates observed here may be due to small changes in position and dynamics of mobile structural elements of RNAp that are known to affect elongation rates. Since heterogeneity persists throughout our experiments and is reversible in some cases, we speculate that *cis-trans* isomerization of a Pro residue could explain the observed switch. The effects of proline isomers mimic those of residue substitutions (Wedemeyer et al., 2002), and substitutions of prolines in two hinges of the *E. coli* RNAp TL have been shown to alter the TL dynamics, which in turn control RNAp translocation and pausing (Windgassen et al., 2014). Upon cognate NTP binding, TL refolds into trigger helices (TH) and forms a three-helix bundle with the bridge helix (BH) to position the 3' OH and the NTP substrate for catalysis (Vassylyev et al., 2007). Stabilizing the TH and the SI3 insertion in the TL in the closed conformation inhibits swiveling, and thus the pausing that is associated with swiveling, yet is thought to favor the pre-translocated TEC (Bao and Landick, 2021; Malinen et al., 2012; Windgassen et al., 2014). Consistently, locking the TH and the closed SI3 through disulfide bridges inhibits hairpin-stabilized pausing but promotes pausing at other sites (Bao and Landick, 2021; Windgassen et al., 2014). In our experiments, heterogeneity is associated with short pauses, prompting us to conjecture that it could occur at sites where translocation might be limited by the template sequence. We note, however, that we cannot identify sequences where conformational changes in RNAp structural elements (e.g., clamp, BH, F-loop, and jaw) could lead to infrequent and short-lived pauses.

An additional source of heterogeneity is linked to significant differences in long-lived pause lifetimes associated with backtracked TEC. A minority subpopulation of RNAp ($\sim$10%) showed notably slower backtrack-recovery rates from both the P2 and the P3 states, indicating a slower intrinsic cleavage rate. We note that the longest pause durations in this subpopulation exceed thousands of seconds, and have been previously categorized as arrested states unable to recover from backtrack (Davenport, 2000; Forde et al., 2002; Galburt et al., 2009; Mejia et al., 2008; Miropolskaya et al., 2017; Tetone et al., 2017). Since many structural elements involved in RNA synthesis also participate in the RNA cleavage, we assume that the suggested possible chemical modification of different structure motifs during RNAp synthesis may also be responsible for the observed RNA cleavage-deficient subpopulation. Elucidating the microscopic origin and cause of the observed different dynamic RNAp behavior remains an important subject for future biochemical and structural studies.

Limitations of the study

Due to limits on the spatiotemporal resolution of the employed methodology, a limitation of the study is the inability to differentiate between shallow backtracked and EP states as well as to detect pause states that are short-lived and infrequent in order to interrogate their potential sequence dependence. The methodological approach can also not detect structural transitions (i.e., in clamp, BH, F-loop, jaw, TH) that lead to—or exist in—individual pause states.

STAR★METHODS

Detailed methods are provided in the online version of this paper and include the following:

- KEY RESOURCES TABLE
- RESOURCE AVAILABILITY
  - Lead contact
  - Materials availability
  - Data and code availability
- METHOD DETAILS
  - Purification of *E. coli* RNApholoenzyme and Gre factors A and B
  - DNA constructs for single-molecule experiments
  - M1: single-molecule RNAp transcription assay
  - M2: magnetic tweezers instrumentation
  - M3: statistical DWT analysis of RNAp transcription trajectories
  - M4: selection of RNAp transcription trajectories based on Gaussian mixture model
  - M5: decomposition of the theoretical dwell-time distribution into exponential processes
  - M6: Estimation of the model parameters and number of kinetic states
  - M7: validation of the ML fit to the reference dataset
  - M8: characterizing the change in model parameters at modulated empirical conditions
  - M9: the dependence of pause probability and effective elongation rate on NTP concentration and external force
  - M10: Parameter estimation for the diffusive backtracking model
- QUANTIFICATION AND STATISTICAL ANALYSIS

SUPPLEMENTAL INFORMATION

Supplemental information can be found online at https://doi.org/10.1016/j.celrep.2022.110749.

AUTHOR CONTRIBUTIONS

R.J., B.E.M., I.A., M.D., and N.H.D. designed the experiments. R.J. performed the single-molecule experiments and processed data. B.E.M. and M.D. designed the analysis pipeline, and B.E.M. performed the dwell-time analysis and *in silico* modeling. All authors contributed to the written manuscript.

DECLARATION OF INTERESTS

The authors declare no competing interests.

REFERENCES

Abbondanzieri, E.A., Greenleaf, W.J., Shaevitz, J.W., Landick, R., and Block, S.M. (2005a). Direct observation of base-pair stepping by RNA polymerase. Nature *438*, 460–465.

Abbondanzieri, E.A., Shaevitz, J.W., and Block, S.M. (2005b). Picocalorimetry of transcription by RNA polymerase. Biophys. J. *89*, L61–L63.

Abdelkareem, M., Saint-André, C., Takacs, M., Papai, G., Crucifix, C., Guo, X., Ortiz, J., and Weixlbaumer, A. (2019). Structural basis of transcription: RNA polymerase backtracking and its reactivation. Mol. Cell *75*, 298–309.e4.

Adelman, K., La Porta, A., Santangelo, T.J., Lis, J.T., Roberts, J.W., and Wang, M.D. (2002a). Single molecule analysis of RNA polymerase elongation reveals uniform kinetic behavior. Proc. Natl. Acad. Sci. U S A *99*, 13538–13543.

Adelman, K., La Porta, A., Santangelo, T.J., Lis, J.T., Roberts, J.W., and Wang, M.D. (2002b). Single molecule analysis of RNA polymerase elongation reveals uniform kinetic behavior. Proc. Natl. Acad. Sci. U S A *99*, 13538–13543.

Artsimovitch, I., and Landick, R. (2000). Pausing by bacterial RNA polymerase is mediated by mechanistically distinct classes of signals. Proc. Natl. Acad. Sci. U S A *97*, 7090–7095.

Bao, Y., and Landick, R. (2021). Obligate movements of an active site–linked surface domain control RNA polymerase elongation and pausing via a Phe pocket anchor. Proc. Natl. Acad. Sci. U S A *118*, e2101805118.

Bar-Nahum, G., Epshtein, V., Ruckenstein, A.E., Rafikov, R., Mustaev, A., and Nudler, E. (2005). A ratchet mechanism of transcription elongation and its control. Cell *120*, 183–193.

Belogurov, G.A., and Artsimovitch, I. (2019). The mechanisms of substrate selection, catalysis, and translocation by the elongating RNA polymerase. J. Mol. Biol. *431*, 3975–4006.

Biernacki, C., Celeux, G., and Govaert, G. (2000). Assessing a mixture model for clustering with the integrated completed likelihood. IEEE Trans. Pattern Anal. Mach. Intell. *22*, 719–725.

Borukhov, S., Sagitov, V., and Goldfarb, A. (1993). Transcript cleavage factors from E. coli. Cell *72*, 459–466.

Bouchiat, C., Wang, M.D., Allemand, J.-F., Strick, T., Block, S.M., and Croquette, V. (1999). Estimating the persistence length of a worm-like chain molecule from force-extension measurements. Biophys. J. *76*, 409–413.

Chamberlin, M.J., Nierman, W.C., Wiggs, J., and Neff, N. (1979). A quantitative assay for bacterial RNA polymerases. J. Biol. Chem. *254*, 10061–10069.

Cnossen, J.P., Dulin, D., and Dekker, N.H. (2014). An optimized software framework for real-time, high-throughput tracking of spherical beads. Rev. Sci. Instrum. *85*, 103712.

Dangkulwanich, M., Ishibashi, T., Bintu, L., and Bustamante, C. (2014). Molecular mechanisms of transcription through single-molecule experiments. Chem. Rev. *114*, 3203–3223.

Davenport, R.J. (2000). Single-molecule study of transcriptional pausing and arrest by E. coli RNA polymerase. Science *287*, 2497–2500.

Depken, M., Galburt, E.A., and Grill, S.W. (2009). The origin of short transcriptional pauses. Biophys. J. *96*, 2189–2193.

Dulin, D., Berghuis, B.A., Depken, M., and Dekker, N.H. (2015a). Untangling reaction pathways through modern approaches to high-throughput single-molecule force-spectroscopy experiments. Curr. Opin. Struct. Biol. *34*, 116–122.

Dulin, D., Vilfan, I.D., Berghuis, B.A., Hage, S., Bamford, D.H., Poranen, M.M., Depken, M., and Dekker, N.H. (2015b). Elongation-competent pauses govern the fidelity of a viral RNA-dependent RNA polymerase. Cell Rep. *10*, 983–992.

Ederth, Josefine, Artsimovitch, Irina, Isaksson, Leif, A, and Landick, Robert (2002). The Downstream DNA Jaw of Bacterial RNA Polymerase Facilitates

Both Transcriptional Initiation and Pausing. Journal of Biological Chemistry *277* (*40*), 37456–37463. https://doi.org/10.1074/jbc.M207038200.

Forde, N.R., Izhaky, D., Woodcock, G.R., Wuite, G.J.L., and Bustamante, C. (2002). Using mechanical force to probe the mechanism of pausing and arrest during continuous elongation by Escherichia coli RNA polymerase. Proc. Natl. Acad. Sci. U S A *99*, 11682–11687.

Gabizon, R., Lee, A., Vahedian-Movahed, H., Ebright, R.H., and Bustamante, C.J. (2018). Pause sequences facilitate entry into long-lived paused states by reducing RNA polymerase transcription rates. Nat. Commun. *9*, 2930.

Galburt, E.A., Grill, S.W., Wiedmann, A., Lubkowska, L., Choy, J., Nogales, E., Kashlev, M., and Bustamante, C. (2007). Backtracking determines the force sensitivity of RNAP II in a factor-dependent manner. Nature *446*, 820–823.

Galburt, E.A., Grill, S.W., and Bustamante, C. (2009). Single molecule transcription elongation. Methods *48*, 323–332.

Gillespie, D.T. (1976). A general method for numerically simulating the stochastic time evolution of coupled chemical reactions. J. Comput. Phys. *22*, 403–434.

Guo, X., Myasnikov, A.G., Chen, J., Crucifix, C., Papai, G., Takacs, M., Schultz, P., and Weixlbaumer, A. (2018). Structural basis for NusA stabilized transcriptional pausing. Mol. Cell *69*, 816–827.e4.

Harrington, K.J., Laughlin, R.B., and Liang, S. (2001). Balanced branching in transcription termination. Proc. Natl. Acad. Sci. U S A *98*, 5019–5024.

Herbert, K.M., La Porta, A., Wong, B.J., Mooney, R.A., Neuman, K.C., Landick, R., and Block, S.M. (2006). Sequence-resolved detection of pausing by single RNA polymerase molecules. Cell *125*, 1083–1094.

Janissen, R., Arens, M.M.A., Vtyurina, N.N., Rivai, Z., Sunday, N.D., Eslami-Mossallam, B., Gritsenko, A.A., Laan, L., de Ridder, D., Artsimovitch, I., et al. (2018). Global DNA compaction in stationary-phase bacteria does not affect transcription. Cell *174*, 1188–1199.e14.

Kang, J.Y., Mishanina, T.V., Bellecourt, M.J., Mooney, R.A., Darst, S.A., and Landick, R. (2018). RNA polymerase accommodates a pause RNA hairpin by global conformational rearrangements that prolong pausing. Mol. Cell *69*, 802–815.e5.

Kang, J.Y., Mishanina, T.V., Landick, R., and Darst, S.A. (2019). Mechanisms of transcriptional pausing in bacteria. J. Mol. Biol. *431*, 4007–4029.

Komissarova, N., and Kashlev, M. (1997). Transcriptional arrest: Escherichia coli RNA polymerase translocates backward, leaving the 3' end of the RNA intact and extruded. Proc. Natl. Acad. Sci. U S A *94*, 1755–1760.

Kwak, H., and Lis, J.T. (2013). Control of transcriptional elongation. Annu. Rev. Genet. *47*, 483–508.

Larson, M.H., Landick, R., and Block, S.M. (2011). Single-molecule studies of RNA Polymerase: one singular sensation, every little step it takes. Mol. Cell *41*, 249–262.

Larson, M.H., Mooney, R.A., Peters, J.M., Windgassen, T., Nayak, D., Gross, C.A., Block, S.M., Greenleaf, W.J., Landick, R., and Weissman, J.S. (2014). A pause sequence enriched at translation start sites drives transcription dynamics in vivo. Science *344*, 1042–1047.

Lass-Napiorkowska, A., and Heyduk, T. (2016). Real-time observation of backtracking by bacterial RNA polymerase. Biochemistry *55*, 647–658.

Lee, J., and Borukhov, S. (2016). Bacterial RNA polymerase-DNA Interaction—the driving force of gene expression and the target for drug action. Front. Mol. Biosci. *3*, 73.

Lisica, A., Engel, C., Jahnel, M., Roldán, É., Galburt, E.A., Cramer, P., and Grill, S.W. (2016). Mechanisms of backtrack recovery by RNA polymerases I and II. Proc. Natl. Acad. Sci. U S A *113*, 2946–2951.

Maizels, N.M. (1973). The nucleotide sequence of the lactose messenger ribonucleic acid transcribed from the UV5 promoter mutant of Escherichia coli. Proc. Natl. Acad. Sci. U S A *70*, 3585–3589.

Malinen, A.M., Turtola, M., Parthiban, M., Vainonen, L., Johnson, M.S., and Belogurov, G.A. (2012). Active site opening and closure control translocation of multisubunit RNA polymerase. Nucleic Acids Res. *40*, 7442–7451.

Markovtsov, V., Mustaev, A., and Goldfarb, A. (1996). Protein-RNA interactions in the active center of transcription elongation complex. Proc. Natl. Acad. Sci. U S A *93*, 3221–3226.

Mejia, Y.X., Mao, H., Forde, N.R., and Bustamante, C. (2008). Thermal probing of E. coli RNA polymerase off-pathway mechanisms. J. Mol. Biol. *382*, 628–637.

Mejia, Y.X., Nudler, E., and Bustamante, C. (2015). Trigger loop folding determines transcription rate of Escherichia coli's RNA polymerase. Proc. Natl. Acad. Sci. U S A *112*, 743–748.

Miropolskaya, N., Esyunina, D., and Kulbachinskiy, A. (2017). Conserved functions of the trigger loop and Gre factors in RNA cleavage by bacterial RNA polymerases. J. Biol. Chem. *292*, 6744–6752.

Neuman, K.C., Abbondanzieri, E.A., Landick, R., Gelles, J., and Block, S.M. (2003). Ubiquitous transcriptional pausing is independent of RNA polymerase backtracking. Cell *115*, 437–447.

Nudler, E., Avetissova, E., Markovtsov, V., and Goldfarb, A. (1996). Transcription processivity: protein-DNA interactions holding together the elongation complex. Science *273*, 211–217.

Ó Maoiléidigh, D., Tadigotla, V.R., Nudler, E., and Ruckenstein, A.E. (2011). A unified model of transcription elongation: what have we learned from single-molecule experiments? Biophys. J. *100*, 1157–1166.

Ostrofet, E., Papini, F.S., and Dulin, D. (2018). Correction-free force calibration for magnetic tweezers experiments. Sci. Rep. *8*, 15920.

Prajapati, R.K., Rosenqvist, P., Palmu, K., Mäkinen, J.J., Malinen, A.M., Virta, P., Metsä-Ketelä, M., and Belogurov, G.A. (2019). Oxazinomycin arrests RNA polymerase at the polythymidine sequences. Nucleic Acids Res. *47*, 10296–10312.

Press, W.H., Teukolsky, S.A., Vetterling, W.T., and Flannery, B.P. (2007). Numerical Recipes Third edition: The Art of Scientific Computing, 3rd (Cambridge University Press).

Pupov, D.V., Barinova, N.A., and Kulbachinskiy, A.V. (2008). Analysis of RNA cleavage by RNA polymerases from Escherichia coli and Deinococcus radiodurans. Biochem 73, 725–729.

Saba, J., Chua, X.Y., Mishanina, T.V., Nayak, D., Windgassen, T.A., Mooney, R.A., and Landick, R. (2019). The elemental mechanism of transcriptional pausing. Elife *8*, e40981.

Schwarz, G. (1978). Estimating the dimension of a model. Ann. Stat. *6*, 461–464.

Sekine, S., Murayama, Y., Svetlov, V., Nudler, E., and Yokoyama, S. (2015). The ratcheted and ratchetable structural states of RNA polymerase underlie multiple transcriptional functions. Mol. Cell *57*, 408–421.

Shaevitz, J.W., Abbondanzieri, E.A., Landick, R., and Block, S.M. (2003). Backtracking by single RNA polymerase molecules observed at near-base-pair resolution. Nature *426*, 684–687.

Sosunova, E., Sosunov, V., Epshtein, V., Nikiforov, V., and Mustaev, A. (2013). Control of transcriptional fidelity by active center tuning as derived from RNA polymerase endonuclease reaction. J. Biol. Chem. *288*, 6688–6703.

Svetlov, V., and Artsimovitch, I. (2015). Purification of bacterial RNA polymerase: tools and protocols. Methods Mol. Biol. *1276*, 13–29.

Tetone, L.E., Friedman, L.J., Osborne, M.L., Ravi, H., Kyzer, S., Stumper, S.K., Mooney, R.A., Landick, R., and Gelles, J. (2017). Dynamics of GreB-RNA polymerase interaction allow a proofreading accessory protein to patrol for transcription complexes needing rescue. Proc. Natl. Acad. Sci. U S A *114*, E1081–E1090.

Tolić-Nørrelykke, S.F., Engh, A.M., Landick, R., and Gelles, J. (2004). Diversity in the rates of transcript elongation by single RNA polymerase molecules. J. Biol. Chem. *279*, 3292–3299.

Vassylyev, D.G., Vassylyeva, M.N., Zhang, J., Palangat, M., Artsimovitch, I., and Landick, R. (2007). Structural basis for substrate loading in bacterial RNA polymerase. Nature *448*, 163–168.

Vassylyeva, M.N., Svetlov, V., Dearborn, A.D., Klyuyev, S., Artsimovitch, I., and Vassylyev, D.G. (2007). The carboxy-terminal coiled-coil of the RNA

polymerase β′-subunit is the main binding site for Gre factors. EMBO Rep. *8*, 1038–1043.

Wedemeyer, W.J., Welker, E., and Scheraga, H.A. (2002). Proline Cis−trans isomerization and protein folding. Biochemistry *41*, 14637–14644.

Windgassen, T.A., Mooney, R.A., Nayak, D., Palangat, M., Zhang, J., and Landick, R. (2014). Trigger-helix folding pathway and SI3 mediate catalysis and hairpin-stabilized pausing by Escherichia coli RNA polymerase. Nucleic Acids Res. *42*, 12707–12721.

Yin, H., Wang, M.D., Svoboda, K., Landick, R., Block, S.M., and Gelles, J. (1995). Transcription against an applied force. Science *270*, 1653–1657.

Yuzenkova, Y., and Zenkin, N. (2010). Central role of the RNA polymerase trigger loop in intrinsic RNA hydrolysis. Proc. Natl. Acad. Sci. U S A *107*, 10878–10883.

Yuzenkova, Y., Bochkareva, A., Tadigotla, V.R., Roghanian, M., Zorov, S., Severinov, K., and Zenkin, N. (2010). Stepwise mechanism for transcription fidelity. BMC Biol. *8*, 54.

Zhang, J., Palangat, M., and Landick, R. (2010). Role of the RNA polymerase trigger loop in catalysis and pausing. Nat. Struct. Mol. Biol. *17*, 99–104.

Zlatanova, J., McAllister, W.T., Borukhov, S., and Leuba, S.H. (2006). Single-Molecule approaches reveal the idiosyncrasies of RNA polymerases. Structure *14*, 953–966.

STAR★METHODS

KEY RESOURCES TABLE

REAGENT or RESOURCE	SOURCE	IDENTIFIER
Antibodies		
Digoxigenin antibodies	Roche	RRID: AB_514496
Chemicals, peptides, and recombinant proteins		
ApU dinucleotide	IBA Lifesciences GmbH	Cat# 0-31004
GpU dinucleotide	TriLink Biotechnologies	Cat# 0-31012
Biotin-16-dUTP	Roche	Cat# 11093711103
Digoxigenin-11-dUTP	Roche	Cat# 11093681103
rNTPs	GE Healthcare	Cat# 27-2025-01
Streptavidin-coated superparamagnetic beads	Thermo Fischer	Cat# 65001
Biotinylated *E. coli* RNA polymerase	Svetlov and Artsimovitch, 2015	N/A
E. coli σ^{70}	Svetlov and Artsimovitch, 2015	N/A
GreA	Vassylyeva et al., 2007	N/A
GreB	Vassylyeva et al., 2007	N/A
Oligonucleotides		
GACCGAGATAGGGTTGAGTG	IDT	1
CATCTTGGTCTCCCCTACGCTCTAGAACTAGTGGATCCCCC	IDT	2
CCATCTTGGTCTCCTAGGCGTCAGCCTGCGAAGCAGTGGC	IDT	3
CCATCTTGGTCTCCTGTCAACACCACTTTGCTCCGAGGTT	IDT	4
CCATCTTGGTCTCCGACAGCGCCATTCGCCATTCAGGCTG	IDT	5
CTTCTGCTTTCCTGATGCAAAAAC	IDT	6
CTGCGGTCTCGCCCGACCGGCTCCAGATTTATCAGC	IDT	7
CTGCGGTCTCGTCAAAAACTGGAACAACACTCAACCC	IDT	8
CTGCGGTCTCGTAGGAGGCGCCATTCGCCATTCAGG	IDT	9
CTGCGGTCTCGCCGGGTTGCAGCACTGGGGCCAGATG	IDT	10
Recombinant DNA		
pIA146: transcription elongation template	Ederth et al., 2002	N/A
pIA586: σ^{70} expression vector	Svetlov and Artsimovitch, 2015	N/A
pIA1202: RNAP expression vector β'AVI-tag-TEV [His$_7$]	Svetlov and Artsimovitch, 2015	N/A
pVS10: RNAP expression vector β'[His$_7$]	Svetlov and Artsimovitch, 2015	N/A
Software and algorithms		
MATLAB R13	MathWorks Inc.	RRID: SCR_001622
Igor Pro 6.37	Wavemetrics	RRID: SCR_000325
LabView 2011	National Instruments	RRID: SCR_014325

RESOURCE AVAILABILITY

Lead contact

Further information and requests for resources and reagents should be directed to and will be fulfilled by the lead contact, Nynke H. Dekker (n.h.dekker@tudelft.nl).

Materials availability

This study did not generate new unique reagents.

Data and code availability

- The single-molecule data reported in this study cannot be deposited in a public repository because they do not follow any standardized datatype. The single-molecule data reported in this paper will be shared by the Lead contact upon request.

- This paper does not report original code.
- Any additional information required to reanalyze the data reported in this paper is available from the Lead contact upon request.

METHOD DETAILS

Purification of *E. coli* RNApholoenzyme and Gre factors A and B

Wild-type *E. coli* RNAp holoenzyme with pre-bound transcription factor δ^{70} was purified as previously described (Svetlov and Artsimovitch, 2015). The enzyme contains a biotin-modification at the β'-subunit that serves as an anchor to attach streptavidin-coated magnetic beads (Abbondanzieri et al., 2005a). GreA and GreB factors were individually obtained and purified following a previously established protocol (Vassylyeva et al., 2007). The activity of all purified proteins was confirmed using standard bulk transcription assays.

DNA constructs for single-molecule experiments

To create a digoxigenin (DIG)-enriched handle, a 643 bp fragment from pBluescript Sk+ (Stratagene, Agilent Technologies Inc., USA) was amplified by PCR in the presence of Digoxigenin-11-dUTP (Roche Diagnostics, Switzerland) using primers 1 and 2 (Table S3). Oligonucleotides (Table S3) were obtained from Ella Biotech GmbH, Germany.

For the assisting force (AF) configuration, the digoxigenin-enriched DIG handle was ligated to a 4015 bp spacer consisting of lambda phage sequence from the plasmid pblue1,2,4 + pSFv1A using primers 3 and 4 (Table S3) followed by the T7A1 promoter in front of the *rpoB* coding sequence and the T7 terminator derived by PCR using plasmid pIA146 and primers 5 and 6 (Table S3). This resulted in a linear dsDNA construct of 9.2 kb.

For the opposing force (OF) configuration, the T7 terminator site was removed from plasmid pIA146 by digesting the plasmid with *Hind*III and *Sph*I (New England Biolabs, UK). Blunt ends were created using the Klenow fragment of DNA polymerase I (New England Biolabs, UK), and these blunt ends were ligated together with T4 DNA ligase (New England Biolabs, UK), resulting in plasmid pIA146-Δterminator. DIG handles were ligated to a 1268 bp PCR fragment from plasmid pIA146Δterminator using primers 7 and 8 (Table S3) and a 5543 bp PCR fragment from plasmid pIA146 using primers 9 and 10 (Table S3). Prior to ligations, all amplicons were digested with the non-palindromic restriction enzyme *Bsa*I-HF (New England Biolabs, UK). The ligation of the fragments was carried out using T4 DNA ligase (New England Biolabs, UK). This resulted in a linear dsDNA construct of 7.5 kb.

M1: single-molecule RNAp transcription assay

The flow cell preparation used in this study has been described in detail elsewhere (Janissen et al., 2018). In short, polystyrene reference beads (Polysciences Europe) of 1.5 μm in diameter were diluted 1:1500 in PBS buffer (pH 7.4) and then adhered to the nitrocellulose-coated (Invitrogen) surface of the flow cell. Further, digoxigenin antibody Fab fragments (Roche Diagnostics) at a concentration of 0.5 mg/mL were incubated for ~1 h within the flow cell, following incubation for ~2 h of 10 mg/mL BSA (New England Biolabs) diluted in buffer A containing 20 mM Tris, 100 mM KCl, 10 mM MgCl$_2$, 0.05% (v/v) Tween 20 (Sigma Aldrich) and 40 μg/mL BSA (New England Biolabs), adjusted to pH 7.9.

The preparation of the RNAp ternary complex was performed as described previously (Abbondanzieri et al., 2005a; Janissen et al., 2018). Briefly, RNAp holoenzyme was stalled on the DNA constructs at position A29 after the T7A1 promoter sequence. To do so, 3 nM of RNAp holoenzyme (with δ^{70}) was added to 3 nM linear DNA template in buffer A and incubated 10 min at 37°C. Afterward, 50 μM ATP, CTP, GTP (GE Healthcare Europe), and 100 μM ApU (IBA Lifesciences GmbH) were added to the solution and incubated for additional 10 min at 30°C. To ensure that we measured the transcription dynamics of single RNAp ternary complexes, we sequestered free RNAp and RNAp that were weakly associated with the DNA by adding heparin to a final concentration of 100 μg/mL and incubating for 10 min at 30°C. Afterward, the ternary complex solution was diluted to a final concentration of 250 pM of the RNAp:DNA complex. The complex was flushed into the flow cell and incubated for 30 min at room temperature. The subsequent addition of 100 μL streptavidin-coated superparamagnetic beads (diluted 1:400 in PBS buffer; MyOne #65601 Dynabeads, Invitrogen/Life Technologies) with a diameter of 1 μm resulted in the attachment of the beads to biotinylated RNAp stalled on the DNA.

Transcription was re-initiated by adding ATP, CTP, GTP, and UTP (GE Healthcare Europe) to buffer A at equimolar concentration of 1 mM to the stalled RNAp ternary complexes and immediately starting the single-molecule measurements. The experiments were conducted for 2.5 h at constant pulling forces with a camera acquisition rate of 25 Hz. Instrumental drift was excluded by the use of surface-attached reference beads.

Transcription traces were processed using custom-written Igor v6.37 and MATLAB R2016b-based custom-written scripts. The absolute z-position of the RNAp during the transcription process was converted to transcribed RNA product as a function of time, using the end-to-end length determined by the extensible worm-like chain model with an experimentally determined stretch modulus of 800 pN and a persistence length of 56 nm (Bouchiat et al., 1999). To reduce the effect of Brownian noise in the applied DWT analysis and MLE fitting, all elongation traces were filtered prior to 1 Hz using a sliding mean average filter.

M2: magnetic tweezers instrumentation

The magnetic tweezers implementation used in this study has been described previously (Janissen et al., 2018). Briefly, light transmitted through the sample was collected by a 50x oil-immersion objective (CFI Plan 50XH, Achromat; 50x; NA = 0.9, Nikon) and

projected onto a 12-megapixel CMOS camera (#FA-80-12M1H, Falcon2; Teledyne Dalsa) with a sampling frequency of 25 Hz. The applied magnetic field was generated by a pair of vertically aligned permanent neodymium-iron-boron magnets (Webcraft GmbH, Germany) separated by a distance of 1 mm, suspended on a motorized stage (#M-126.PD2, Physik Instrumente) above the flow cell. Additionally, the magnet pair can be rotated around the illumination axis by an applied DC servo step motor (C-150.PD; Physik Instrumente). Image processing of the collected light allowed us to track the real-time position of both surface attached reference beads and superparamagnetic beads coupled to RNAp in three dimensions over time. The bead x, y, z position tracking was achieved using a cross-correlation algorithm realized with custom-written software in LabView (2011, National Instruments Corporation) (Cnossen et al., 2014). The software determined the bead positions with spectral corrections to correct for camera blur and aliasing.

M3: statistical DWT analysis of RNAp transcription trajectories

The transcription dynamics of *E. coli* RNAp were quantitatively assessed using unbiased dwell time analysis (Dulin et al., 2015a; Janissen et al., 2018). In this approach, the times needed for RNAp to transcribe through consecutive dwell time windows of a chosen size - defined as *dwell times* (DWT) - were calculated for all RNAp trajectories and used to construct a DWT probability distribution function. Since the validation of different dwell-time windows does not affect the analysis (Methods M6, Figure S2), we chose a DWT-window of 4 nt and data filtering to 1 Hz filtering for analysis of all datasets within this work. The expected error (standard deviation)in the constructed distribution was estimated by bootstrapping the data 100–1,000 times (Dulin et al., 2015a; Janissen et al., 2018; Press et al., 2007).

M4: selection of RNAp transcription trajectories based on Gaussian mixture model

To select a homogeneous ensemble, a preselection protocol was applied to each dataset, where a Gaussian mixture model were used to classify the transcription trajectories into three clusters, based on the value of the largest pause (or DWT) that was measured for each trajectory (Biernacki et al., 2000). The trajectories associated to the cluster with the largest mean were excluded.

M5: decomposition of the theoretical dwell-time distribution into exponential processes

In this section an analytical expression is derived which is used to fit our proposed model to the reference dataset. To achieve this, certain assumptions and approximations have to be made as described below. We validate these assumptions in section M7 using computer simulation, proving that the analytical expression indeed captures the data well.

Assuming a DWT-window of 1 nt, the DWT distribution as predicted by the model (Figure 2, rightmost panel), can be decomposed into four separate terms,

$$\Psi^{(1)}(t) = \Psi_0^{(1)}(t) + \Psi_1^{(1)}(t) + \Psi_2^{(1)}(t) + \Psi_3^{(1)}(t), \tag{Equation S1}$$

where $\Psi_0^{(1)}(t)$ corresponds to RNAp taking a step without entering the pause pathway, $\Psi_1^{(1)}(t)$ includes entering P1 at least once without entering P2 or P3, $\Psi_2^{(1)}(t)$ includes transitions into P2 without entering P3 and $\Psi_3^{(1)}(t)$ captures transitions into P3. Defining the exponential distributions,

$$\phi_0(t) \approx k_{el} \exp(-k_{el}t), \quad \phi_1(t) = (k_{e1} + k_{p2})\exp(-(k_{e1} + k_{p2})t),$$

$$\phi_2(t) = (k_{e2} + k_{p3})\exp(-(k_{e1} + k_{p2})t), \quad \phi_3(t) = k_{e3} \exp(-k_{e3}t). \tag{Equation S2}$$

which describe the distribution of the lifetime of the various states in the model, as well as the splitting probabilities,

$$p_2 = \frac{k_{p2}}{(k_{e1} + k_{p2})}, \, p_3 = \frac{k_{p3}}{(k_{e2} + k_{p3})}, \tag{Equation S3}$$

an analytical expression can be found for each component of Equation (S1) in the Laplace space. Denoting the Laplace transformation of a function $f(t)$ as $\tilde{f}(s) = \int_0^\infty f(t)\exp(-st)dt$, we have

$$\tilde{\Psi}_0^{(1)}(s) = (1 - P_{total})\tilde{\phi}_0(s). \tag{Equation S4}$$

Furthermore, defining

$$\psi(s) \equiv \sum_{j=0}^\infty (P_{total}(1 - p_2)\tilde{\phi}_1(s))^j = (1 - P_{total}(1 - p_2)\tilde{\phi}_1(s))^{-1}, \tag{Equation S5}$$

and assuming that the rate into the pause branch is much faster than the pause exit rates, one can write

$$\tilde{\Psi}_1^{(1)}(s) = \psi(s)P_{total}(1 - p_2)\tilde{\phi}_1(s)(1 - P_{total})\tilde{\phi}_0(s), \tag{Equation S6}$$

where the j_{th} term in the sum in Equation (S5) accounts for j successive back-and-forth transitions between the active state and P1 without entering P2. Therefore, Equation (S6) captures all possible ways of RNAp visiting P1 (and not P2 or P3) before taking one step forward.

Similar expressions can be derived for $\tilde{\Psi}_2$ and $\tilde{\Psi}_3$, which are simplified assuming that P2 and P3 are visited at most once per step. This assumption is justified since the probability of entering P2 is estimated to be as low as ~ 0.006 in the reference dataset. Within this limit we obtain

$$\tilde{\Psi}_2^{(1)}(s) \ = \ \psi(s)P_{\text{total}}\,p_2\tilde{\phi}_1(s)(1 - p_3)\tilde{\phi}_2(s)\psi(s)(1 - P_{\text{total}})\tilde{\phi}_0(s), \qquad \text{(Equation S7)}$$

$$\tilde{\Psi}_3^{(1)}(s) \ = \ \psi(s)P_{\text{total}}\,p_2\tilde{\phi}_1(s)p_3\tilde{\phi}_2(s)\tilde{\phi}_3(s)\psi(s)(1 - P_{\text{total}})\tilde{\phi}_0(s). \qquad \text{(Equation S8)}$$

The term $\psi(s)$ appears twice in Equations (S7) and (S8), accounting for back-and-forth transitions between the active state and P1 before and after entering P2, respectively.

Considering that the pause lifetimes, as estimated from the data, are well separated and much slower than the effective elongation rate (Table S2), each term in Equation (S1) can be well approximated with a single exponential,

$$\Psi_i^{(1)}(t) \approx q_i \exp(-k_i t) \quad i = 0, 1, 2, 3, \qquad \text{(Equation S9)}$$

where q_i and k_i are the associated occurrence probabilities and effective rates respectively, and are related to the Laplace transform of $\Psi_i^{(1)}(t)$ via the following equations:

$$q_i \ = \ \tilde{\Psi}_2^{(1)}(s = 0), \quad k_i^{-1} \ = \ -\frac{\partial}{\partial s}\log\tilde{\Psi}_2^{(1)}(s)|_{s = 0}. \qquad \text{(Equation S10)}$$

Considering that the Laplace transformation of an exponential function $\phi(t) = k\exp(-kt)$ is given by $\tilde{\phi}(s) = \frac{k}{s+k}$, from Equations (S5, S6, S7, and S8) we obtain

$$q_0 \ = \ (1 - P_{\text{total}}), \ q_1 \approx P_{\text{total}}\left(1 - \frac{p_2}{1 - P_{\text{total}}}\right), \ q_2 \approx P_{\text{total}}\frac{p_2(1 - p_3)}{1 - P_{\text{total}}}, \ q_2 \approx P_{\text{total}}\frac{p_2 p_3}{1 - P_{\text{total}}}, \qquad \text{(Equation S11)}$$

and

$$k_0^{-1} \ = \ k_{\text{el}}^{-1},$$

$$k_1^{-1} \ = \ ((1 - P_{\text{total}} + P_{\text{total}}\,p_2)(k_{\text{e1}} + k_{\text{p2}}))^{-1} + k_{\text{el}}^{-1},$$

$$k_2^{-1} \ = \ (k_{\text{e2}} + k_{\text{p3}})^{-1} + \left(\left(\frac{1 - P_{\text{total}} + P_{\text{total}}\,p_2}{1 + P_{\text{total}} - P_{\text{total}}\,p_2}\right)(k_{\text{e1}} + k_{\text{p2}})\right)^{-1} + k_{\text{el}}^{-1},$$

$$k_3^{-1} \ = \ k_{\text{e3}}^{-1} + (k_{\text{e2}} + k_{\text{p3}})^{-1} + \left(\left(\frac{1 - P_{\text{total}} + P_{\text{total}}\,p_2}{1 + P_{\text{total}} - P_{\text{total}}\,p_2}\right)(k_{\text{e1}} + k_{\text{p2}})\right)^{-1} + k_{\text{el}}^{-1}. \qquad \text{(Equation S12)}$$

In obtaining the occurrence probabilities given in Equation (S11) all terms of the order $(P_{\text{total}}p_2)^2$ or greater have been ignored, in accordance with the assumption that multiple entrance to P2 is negligibly rare. This preserves the normalization of $\Psi^{(1)}(t)$, i.e. $\sum_{i=0}^{3} q_i = 1$. Replacing Equation (S9) in Equation (S1) yields

$$\Psi^{(1)}(t) \ = \ \sum_{i=0}^{3} q_i \exp(-k_i t). \qquad \text{(Equation S13)}$$

Equation (S13) can be interpreted as RNAp exhibiting four distinct stepping rates, where at each step the rate k_i is chosen with the probability q_i. While $k_1 = k_{\text{el}}$ corresponds to the pause-free elongation rate, each of the other three stepping rates are dominated by the exit rate from one of pause states in the model, as described in Equation (S12). Considering that k_is are sorted in the decreasing order (i.e. $k_i > k_{i+1}$), this interpretation allows for the generalization of Equation (S1) in the case where the width of the DWT-window, N, is larger than one nucleotide. One can thus describe

$$\Psi^{(N)}(t) \ = \ \sum_{i=0}^{3} \Psi_i^{(N)}(t), \qquad \text{(Equation S14)}$$

with $\Psi_i^{(N)}(t)$ representing the conditional DWT distribution, where every step within the DWT-window is restricted to obtain a rate equal or greater than k_i. For $\Psi_0^{(N)}(t)$, which corresponds to the pause-free elongation with the rate $k_0 = k_{el}$, we have

$$\Psi_0^{(N)}(t) = \left(1 - q_1^c\right)^N \Gamma_N(t|k_0), \tag{Equation S15}$$

where $(1 - q_i^c)$ is the probability of not entering the pause branch, $q_i^c \equiv \sum_{j=i}^{3} q_j$, and the gamma function $\Gamma_n(t|k)$ represents the DWT distribution resulting from n successive steps with the rate k,

$$\Gamma_n(t|k) = \frac{k}{(n-1)!}(kt)^{n-1}\exp(-kt). \tag{Equation S16}$$

For $i \geq 1$, $\Psi_i^{(N)}(t)$ can be decomposed into N separate terms with

$$\Psi_i^{(N)}(t) = \sum_{n=1}^{N} \psi_{in}^{(N)}(t), \tag{Equation S17}$$

where $\psi_{in}^{(N)}(t)$ is conditioned to include exactly n pauses with the rate k_i, while all the other steps in the DWT-window are taken at a rate much greater than k_i. The fact that the stepping rates, as inferred from our data, are well separated, allows for a mean-field approximation for $\psi_{in}^{(N)}$ of the form

$$\psi_{in}^{(N)} = a_{in}^{(N)} \Gamma_n(t - (N-n)\tau_i|k_i), \tag{Equation S18}$$

where $a_{in}^{(N)}$ is the probability of RNAp taking n steps with the rake k_i and $N - n$ steps with a rate faster than k_i,

$$a_{in}^{(N)} = \frac{N!}{(N-n)!n!}\left(1 - q_i^c\right)^{N-n}q_i^n, \tag{Equation S19}$$

and we have included τ_i as the average DWT per step, given that the stepping rate is greater than k_i,

$$\tau_i = \frac{\sum_{j=0}^{i-1}q_j k_j^{-1}}{1 - q_i^c}. \tag{Equation S20}$$

The gamma function $\Gamma_n(t - (N-n)\tau_i|k_i)$ in Equation (S18) accounts for the occurrence of n pauses with the lifetime k_i^{-1}. The shift $(N-n)\tau_i$ in the argument of the function reflects the mean-filed assumption that each of the remaining $(N-n)$ steps contribute to the total DWT by a constant average time τ_i. We assume $\psi_{in}^{(N)} = 0$ for $t < (N-n)\tau_i$.

Taken together, we obtain the following approximate analytical expression for the theoretical DWT distribution,

$$\Psi^{(N)}(t) = \left(1 - q_1^c\right)^N \Gamma_N(t|k_0) + \sum_{i=1}^{3}\sum_{n=1}^{N} \frac{N!}{(N-n)!n!}\left(1 - q_i^c\right)^{N-n}q_i^n \Gamma_n(t - (N-n)\tau_i|k_i), \tag{Equation S21}$$

where k_i s and q_i s are related to the model parameters *via* Equations (S11 and S12). We note that Equation (S21) is reduced to Equation (S13) for $N = 1$.

M6: Estimation of the model parameters and number of kinetic states

We estimated the model parameters *via* a maximum likelihood fit to the reference dataset (7.5 *pN* AF, 1 mM NTPs). Due to the existence of empirical noise, as well as the artifacts induced by the filtering process, Equation (S21) cannot be directly used for fitting the data. While for pauses longer than the filtering time the noise artifacts can be suppressed by choosing a wide enough window (in this case 10 nt), the fast pause-free elongation rate, which is represented by the elongation peak in the DWT distribution, is significantly affected. In this case the elongation peak cannot be accurately described by a gamma function. We therefore kept the second term in Equation (S21) to model the contribution from the pauses, but replaced the gamma function $\Gamma_N(t|k_0)$ by a log-normal function which better captures the elongation peak,

$$\Psi^{(N)}(t) = \left(1 - q_1^c\right)^N \Pi(t|\mu, \sigma) + \sum_{i=1}^{3}\sum_{n=1}^{N} \frac{N!}{(N-n)!n!}\left(1 - q_i^c\right)^{N-n}q_i^n \Gamma_n(t - (N-n)\tau_i|k_i), \tag{Equation S22}$$

where

$$\Pi(t|\mu, \sigma) = \frac{1}{\sqrt{2\pi}\sigma t}\exp\left(-\frac{(\ln t - \mu)^2}{2\sigma^2}\right). \tag{Equation S23}$$

We fitted Equation (S22) to the reference data, treating μ and σ as independent fit parameters. This introduces a challenge in estimating the effective elongation rate since an analytical formula which relates μ and σ to k_{el}, and accurately accounts for the noise and filtering artifacts, is not known. We therefore kept k_{el} fixed at an initial guess and estimated all pause exit rates and probabilities

(i.e. $\{k_i.q_i | i = 1.2.3\}$) by fitting Equation (S22) to the reference data. The fit was performed by numerically maximizing the coarse-grained log likelihood function defined as

$$L = \sum_i n_i \log P_i,$$

(Equation S24)

where n_i is the number of DWTs in the i_{th} bin of the empirical DWT distribution, and P_i is the model prediction calculated for that bin. The standard simulated annealing algorithm implemented in MATLAB was used in the optimization.

We then refined our initial guess for the elongation rate by performing a second numerical maximum likelihood fit, taking into account the empirical noise and filtering effects. We note that the elongation rate implicitly enters Equation (S22) through the parameters τ_i s. Our estimations for pause exit rates and probabilities can therefore be potentially affected by our initial guess for the elongation rate. We estimated τ_3 for the reference dataset by measuring the average pause-free velocity, excluding all pauses which are longer than the pause P3 lifetime of ~100 s. This yielded $\tau_3 \sim 0.1$ s, which also serves as an upper bound for τ_1 and τ_2. Therefore, for $N = 10$ we have $N\tau_i \leq 1$ s, which is negligible compared to the estimated pause lifetimes of ~ 5 s and ~ 100 s for P2 and P3, respectively. This implies that that we can ignore the terms $(N - n)\tau_i$ for $i = 2.3$ in the argument of the gamma functions in Equation (S22). As a result, we concluded that our estimations for k_2, k_3, q_2 and q_3 are not significantly affected by our choice of k_{el}, as long as it does not lie far from the correct value. This argument does not necessary hold for the parameters associated with the pause P1, for which we have estimated a lifetime <1 s. Nevertheless, we expect that the estimation for k_1 remains independent of k_{el}, as it is dictated by the exponential decay in the tail of the DWT distribution at short time scales (i.e. between 1–4 s).

In contrast, by simulating DWT distributions from noisy traces (see below), we noticed that the estimation for q_1 is indeed sensitive to the chosen value for k_{el}. Based on this finding, to refine our initial guess for the elongation rate we only used k_{el} and q_1 as free parameters in the numerical maximum likelihood fit, keeping $k_{1.2.3}$ and $q_{2.3}$ at their estimated values resulting from fitting Equation (S22) to the data. The fit was performed *via* grid optimization. For each grid point, an ensemble of trajectories was computationally generated using the Gillespie algorithm (Gillespie, 1976). To achieve an accurate estimation of the effective elongation rate, we included experimental noise. As the empirical noise turned out to be temporally correlated, we employed an ensemble of RNAp pauses exceeding 100 s as the noise source. After adding this noise to the computationally generated trajectories, the trajectories were filtered with a moving average filter of 1 Hz, as in the preprocessing or experimentally RNAp trajectories. The DWT distribution was then constructed from these computationally generated noisy trajectories. This allows for the calculation of the coarse-grained log-likelihood given by Equation (S24), where n_i are the number of DWTs in the i_{th} bin of the empirical DWT distribution, and P_i is the simulated DWT distribution calculated for that bin. The grid points with the largest log-likelihood score yields an estimation for the optimal values of k_{el} and q_1.

Having estimated the complete set of $\{k_i.q_i | i = 0.1.2.3\}$, we calculated all the model parameters by inverting Equations (S11 and S12). Defining $\widehat{k}_1 = k_{e1} + k_{p2}$ and $\widehat{k}_2 = k_{e2} + k_{p3}$, followed by

$$P_{total} = 1 - q_0 = \sum_{i=1}^{3} q_i,$$

$$p_2 = (q_2 + q_3)\frac{(1 - P_{total})}{P_{total}},$$

$$p_3 = \frac{q_3}{q_2 + q_3},$$

(Equation S25)

and

$$\widehat{k}_1 = \left((1 - P_{total} + P_{total}\,p_2)\left(k_1^{-1} - k_{el}^{-1}\right)\right)^{-1},$$

$$\widehat{k}_2 = \left(k_2^{-1} - \left(\left(\frac{1 - P_{total} + P_{total}\,p_2}{1 + P_{total} - P_{total}\,p_2}\right)\widehat{k}_1\right)^{-1} - k_{el}^{-1}\right)^{-1},$$

(Equation S26)

which in combination with Equations (S3) and (S12) followed by

$$k_{e1} = (1 - p_2)\widehat{k}_1,$$

$$k_{p2} = p_2\widehat{k}_1,$$

$$k_{e2} = (1 - p_3)\widehat{k}_2$$

$$k_{p3} = p_3\widehat{k}_2$$

$$k_{e3} = \left(k_3^{-1} - k_2^{-1}\right)^{-1}. \tag{Equation S27}$$

This completes the parameter estimation procedure. To estimate the 1-σ confidence intervals for the model parameters, the data was bootstrapped 100 times and the entire procedure was repeated for each bootstrapped sample.

Equation (S22) can be generalized to describe a generic model, with an arbitrary number of M exponential pauses, by simply setting the upper bound of the first sum in Equation (S22) to M instead of 3. This allowed us to repeat the fit for models with a different number of pause states (e.g. 2–6) and use the Bayesian Information Criteria (BIC) to confirm the existence of three distinct pause states in our data (Dulin et al., 2015a; Schwarz, 1978).

M7: validation of the ML fit to the reference dataset

The reference parameters (Figures 2B and 2C) were obtained by fitting the model to the empirical DWT distribution using a DWT-window of 10 nt. To validate that the choice of the DWT-window does not affect the analysis, the reference parameters were fed to the Gillespie algorithm to computationally generate an ensemble of transcription trajectories as described in M6. The DWT distributions with the window sizes of 4 and 20 nt were then constructed from the computationally generated trajectories and compared to the empirical distributions Figures S2B and S2C.

To confirm that the value obtained for the effective elongation rate k_{el} can be accurately determined by the DWT analysis, it was reevaluated by fitting the pause-free velocity distribution as is commonly used in literature (Dangkulwanich et al., 2014; Galburt et al., 2009). The local velocity of each RNAp trajectory was measured in successive time windows of 1 s, after removing pauses >100 s. These measured velocities were then used to construct the pause-free velocity distribution. The model was then fitted to the distribution by 1-D grid optimization with the effective elongation rate k_{el} as the only free fit parameters (Figures S2E and S2F); all other model parameters are kept fixed at their reference values (Figures 2B and 2C). At each grid point an ensemble of trajectories were computationally generated and the pause-free velocity distribution was constructed. The coarse-grained log-likelihood score was then calculated at each grid point according to Equation (S24), where n_i is the number of velocities in the i_{th} bin of the empirical pause-free velocity distribution, and P_i is the simulated distribution calculated for that bin. The data was bootstrapped and refitted 100 times to estimate the 1-σ confidence interval for the effective elongation rate k_{el}.

To evaluate the variations in the elongation rate k_{el} and pause probability P_{total}, the model was fitted to each individual trajectory in the reference dataset. This was performed by a 2-D grid optimization with k_{el} and P_{total} as free fit parameters; all other model parameters were kept fixed at their reference values (Figures 2B and 2C). For each grid point, the coarse-grained log likelihood score (Equation (S24)) was calculated using simulated noisy elongation trajectories as described in M6. The optimal values for k_{el} and P_{total}, corresponding to the largest score, were then determined, and it was shown that the population-average estimations are consistent with the results from fitting the combined distribution (Figure S3D).

M8: characterizing the change in model parameters at modulated empirical conditions

To fit the empirical DWT distributions measured at low NTP concentrations (i.e. 500 μM, 100 μM, 10 μM, and 1 μM), a 2-D grid optimization of the effective elongation rate k_{el} and pause probability P_{total} was performed by numerically maximizing the coarse-grained log-likelihood score as described in M7. Each RNAp trajectory was fitted individually and the population-averaged values for k_{el} and P_{total} were determined. The uncertainty in the fit outcome was characterized by calculating the standard error of the mean (see Figure 3).

To characterize the force dependency of the P2 pause entry rate, k_{p2}, the model was fitted to the DWT distribution measured at OF 12.5 pN, 1 mM NTPs. The fit was performed in two steps: first, for 11 equally-spaced values of δ in the interval [0,1] the best fit to the data was found using a 2-D grid optimization as described above for low-NTP fits. Each fit was performed using k_{el} and P_{total} as the only free fit parameters; k_{p2} was adjusted according to equation Equation (3) and all the remaining model parameters were kept fixed at their reference values. The log-likelihood score corresponding to the best two-parameter fit was then calculated for each value of δ, and the optimal value of δ = 0.7 corresponding to the largest score was determined. To estimate the uncertainty in δ, the log-likelihood scores were exponentiated and normalized to obtain the probability distribution of δ, from which the 1-σ confidence interval was then calculated (see Figure 4).

For all other externally applied forces (i.e. F = −10, −9, −7.5, −5, 5, 10, 12.5 pN) k_{p2} was adjusted according to Equation (3) using δ = 0.7, and the model was fitted to the empirical DWT distribution using k_{el} and P_{total} as the only free fit parameters, as described above (see Figures 4, S5B, and S5C).

The DWT distribution measured at 9 pN OF served as an individual control for the experiments in presence of GreA or GreB. The fit was performed in two steps. First, only k_{e2} and k_{p3} were considered as free fit parameters, while all other model parameters were fixed according to the best fit to the control data. The optimal values of k_{e2} and k_{p3} were determined by maximizing the coarse-grained log-likelihood score on a 2-D grid, calculated by simulating noisy elongation trajectories as described in M6 and M7. Then, a second maximum likelihood fit was performed on a 1-D grid with k_{e3} as the only free fit parameter. Due to low statistics, the fit was performed on the combined distribution and the data was bootstrapped and refitted 100 times to estimate the 1-σ confidence intervals for the fit outcome (see Figures 5A, 5B, 5C, and 5D).

M9: the dependence of pause probability and effective elongation rate on NTP concentration and external force

The total pause probability, P_{total}, is affected by the sub-processes involved the active pathway. As depicted in Figure S4B, these sub-processes include the transition between pre- and post-translocated states (denoted by 0 and 1, respectively) with the forward rate k_F and the backward rate k_B, the transition to the NTP-bound state (denoted by 2) with the rate k_N, NTP-dissociation with the rate k_D and finally the NTP catalysis with the rate k_C. The catalytic reaction completes the elongation cycle and brings the RNAp back to the next pre-translocated state (denoted by 3), with a new nucleotide added to the RNA chain. Defining p_{ij} as the transition probability between two neighboring sub-states i and $j = i \pm 1$, the probability to complete the elongation cycle without entering the pause branch can be written as

$$P_{03} = \sum_{n,m=0}^{\infty} p_{01} \frac{(n+m)!}{n!m!} (p_{10}p_{01})^n (p_{12}p_{21})^m p_{12}p_{23}. \tag{Equation S28}$$

Equation (S28) accounts for all possible paths from 0 to 3 which do not include entering the pause branch: each path begins with a transition from from 0 to 1 followed by n back-and-forth transitions between 1 and 0 and m back-and-forth transitions between 1 and 2, all ending at 1. The factor $\frac{(n+m)!}{n!m!}$ accounts for all possible permutations for such transitions. A final transition from 1 to 2 followed by a transition from 2 to 3 then completes the catalytic pathway. Using the binomial theorem, Equation (S28) can be simplified as

$$P_{03} = p_{01}p_{12}p_{23} \sum_{k=0}^{\infty} (p_{10}p_{01} + p_{12}p_{21})^k = \frac{p_{01}p_{12}p_{23}}{1 - p_{10}p_{01} - p_{12}p_{21}}. \tag{Equation S29}$$

By definition

$$P_{total} = 1 - P_{03}, \tag{Equation S30}$$

and the probabilities p_{ij} are related to the transition rates as follows

$$p_{01} = \frac{k_F}{k_F + k_p}, \quad p_{12} = 1 - p_{10} = \frac{k_N}{k_N + k_B}, \quad p_{23} = 1 - p_{21} = \frac{k_C}{k_C + k_D}, \tag{Equation S31}$$

Considering that k_N is proportional to the NTP concentration, $k_N = k_N^0[\text{NTPs}]$, Equations (S30), together with Equations (S29) and (S31), yields

$$P_{total} = \frac{P_{min} + \frac{K_p}{[\text{NTPs}]}}{1 + \frac{K_p}{[\text{NTPs}]}}, \tag{Equation S32}$$

where

$$P_{min} = \frac{k_p}{k_F + k_P} \tag{Equation S33}$$

is the lowest value of P_{total} corresponding to a saturating NTPs concentration, and

$$K_p = P_{min} \frac{k_C + k_D}{k_N^0} \cdot \frac{k_B}{k_C}. \tag{Equation S34}$$

The transition rates between the pre- and post-translocated states depend on the external force F as

$$k_f = k_f^0 \exp\left(\frac{F\Delta a}{k_B T}\right), \quad k_b = k_b^0 \exp\left(-\frac{F(1-\Delta)a}{k_B T}\right), \tag{Equation S35}$$

where a is the average step size of RNAp, $0 \leq \Delta \leq 1$ identifies the position of the energy barrier against RNAp transition from the pre-translocated to the post-translocated state, and $k_{f,b}^0$ corresponds to zero force. Assuming that the entry rate to the pause branch, k_{p1}, does not depend on force, using Equations (S33, S34, and S35) we obtain

$$P_{min}(F) = \left[1 + \left(\frac{1}{P_{min}^{ref}} - 1\right) \exp\left(\frac{(F - F^{ref})\Delta a}{k_B T}\right)\right]^{-1},$$

$$K_p(F) = \frac{P_{\min}(F)}{P_{\min}^{ref}}K_p^{ref}\exp\left(-\frac{(F-F^{ref})(1-\Delta)a}{k_BT}\right),$$ (Equation S36)

where $P_{\min}^{ref}$ and K_p^{ref} correspond to a reference force F^{ref}.

An analytical expression can be obtained for the effective elongation rate. We denote the first-passage time distribution of completing one elongation cycle without pausing (i.e. transiting from state 0 to 3 in Figure S4B) by $\Psi_{03}(t)$, and its Laplace transformation by $\tilde{\Psi}_{03}(s) = \int_0 \Psi_{03}(t)\exp(-st)dt$. Similar to Equation (S29) one can write

$$\tilde{\Psi}_{03}(s) = \frac{\tilde{\phi}_{01}(s)\tilde{\phi}_{12}(s)\tilde{\phi}_{23}(s)}{1-\tilde{\phi}_{10}(s)\tilde{\phi}_{01}(s)-\tilde{\phi}_{12}(s)\tilde{\phi}_{21}(s)},$$ (Equation S37)

where $\tilde{\phi}_{ij}(s)$ is the Laplace transformation of the first-passage time distribution for a transition from state i to a neighboring state j,

$$\tilde{\phi}_{01}(s) = \frac{k_F}{s+k_F+k_p}, \quad \tilde{\phi}_{12}(s) = \frac{k_N}{s+k_N+k_B}, \quad \tilde{\phi}_{23}(s) = \frac{k_C}{s+k_C+k_D}$$

$$\tilde{\phi}_{10}(s) = \frac{k_B}{k_N}\tilde{\phi}_{12}(s), \quad \tilde{\phi}_{21}(s) = \frac{k_D}{k_C}\tilde{\phi}_{23}(s), \quad .$$ (Equation S38)

The elongation rate, k_{el}, can then be calculated as

$$k_{el}^{-1} = -\frac{\partial}{\partial s}\log\tilde{\Psi}_{03}(S)\bigg|_{s=0}.$$ (Equation S39)

Using Equation (S38) and defining

$$V_{\max} = \frac{(k_F+k_p)k_C}{k_F+k_p+k_C}, \quad K_m = \frac{(k_F+k_B+k_p)(k_C+k_D)+k_pk_B}{(k_F+k_p+k_C)k_N^0},$$ (Equation S40)

we obtain

$$k_{el} = \left(1+\frac{K_p}{[NTP]}\right)k_{el}^0,$$ (Equation S41)

where K_p is given by Equation (S34) and k_{el}^0 is the elongation rate at $k_p = 0$ which follows the Michaelis-Menten kinetics

$$k_{el}^0 = \frac{V_{max}}{1+\frac{K_m}{[NTP]}}.$$ (Equation S42)

M10: Parameter estimation for the diffusive backtracking model

To model diffusive backtracking, we modified equation Equation (S22) to include one exponential pause with the rate k_1 and probability q_1, as well as a diffusive backtracking pause with the probability q_2, the forward rate k_f, and the backward rate k_b. Assuming $Nq_2 \ll 1$, which is justified for $N = 10$ and $q_2 \sim 0.006$, we obtain

$$\Psi^{(N)}(t) = (1-q_1^c)^N\Pi(t|\mu,\sigma) + \sum_{n=1}^{N}\frac{N!}{(N-n)!n!}(1-q_1^c)^{N-n}q_1^n\Gamma_n(t-(N-n)\tau_1|k_1) + Nq_2\Lambda(t-(N-1)\tau_2|k_f,k_b),$$ (Equation S43)

where $q_i^c \equiv \sum_{j=i}^{2}q_j$, $\tau_{1,2}$ are given by Equation (S20), and $\Lambda(t|k_f.k_b)$ is given by

$$\Lambda(t|k_f,k_b) = \frac{k_f\exp(-(k_f+k_b)t)}{k_0t}I_1(2k_0t),$$ (Equation S44)

with $k_0 = \sqrt{k_fk_b}$, and $I_1(x)$ is the degree one modified Bessel function of the first kind (Depken et al., 2009).

The diffusive backtracking model was fitted to the reference data using a similar procedure as described in M6. First a maximum likelihood fit was performed using Equation (S43), with k_{el} kept fixed at an initial guess. A second maximum likelihood fit via 2-D grid optimization was then performed using q_1 and k_{el} as the only free parameters. While the forward and backward rates k_f, k_b were directly estimated from the fit, estimating k_{el}, k_1, and $q_{1,2}$ allows for adjusting Equations (S25, S26, and S27) to calculate P_{total}, k_{e1}, and kp_{BT} as follows (Figure S6, rightmost panel):

$$P_{total} = q_1+q_2,$$

$$k_{e1} = (1 - p_2)\widehat{k}_1,$$

$$kp_{BT} = p_2\widehat{k}_1, \tag{Equation S45}$$

where $p_2 = q_2\frac{(1 - P_{total})}{P_{total}}$ and $\widehat{k}_1$ is given by Equation (S26). Using the estimated model parameters, the DWT distribution was simulated with limited diffusive backtracking, where the maximum backtrack depth was varied between 3 - 14 nt.

The model was tested on the data measured at OF 12.5 pN and 1 mM NTPs, assuming that the rates associated with backtracking depend on force *via* the following equations:

$$kp_{BT} = kp_{BT}^{ref} \exp\left(-\frac{(F - F^{ref})(1 - \delta)a}{k_B T}\right),$$

$$k_b = k_b^{ref} \exp\left(-\frac{(F - F^{ref})(1 - \delta)a}{k_B T}\right),$$

$$k_f = k_f^{ref} \exp\left(\frac{(F - F^{ref})\delta a}{k_B T}\right) \tag{Equation S46}$$

where $F = -12.5$ pN, $a \approx 0.37$ nm, and the superscript "*ref*" refers to the value of the parameter estimated for the reference data at $F^{ref} = 7.5$ pN. An ensemble of noisy traces was then simulated as described in M6 to construct DWT distributions and calculate the average RNAp processivities for different values of δ and maximum backtrack depth. In all simulations, k_{el} and p_{total} were fixed according to Table S2. The best fit of the diffusive backtracking model to the 12.5 *pN* OF data was find by calculating the coarse-grained log-likelihood score using Equation Equation (S24) for each simulation.

QUANTIFICATION AND STATISTICAL ANALYSIS

The sample statistics of analyzed RNAp trajectories, total transcript lengths, and DWTs are specified in Table S1 for all different conditions tested. The one-sigma confidence intervals in Figures 2B and 2C and Figures 3A and 3B were determined by bootstrapping with 1,000 iterations. Statistical analysis of data shown in Figures 3A and 3B was performed by using one-way ANOVA, with comparative Tukey post-hoc test (significance level α: *** = 0.001; * = 0.05). The data shown in Figures 5B–6G, and in Figures S2F, S5A, and S6B were subject to statistical analysis using unpaired, two-tailed t-tests (p: *** < 0.001;** <0.01; * <0.05; n.s. = non-significant).